Published in "Spectrochimica Acta Part B: Atomic Spectroscopy 88: 136–149, 2014"
which should be cited to refer to this work.

High-energy-resolution grazing emission X-ray fluorescence applied to the characterization of thin Al films on Si

Y. Kayser [a,b,*], J. Szlachetko [b,c], D. Banaś [c], W. Cao [a,d], J.-Cl. Dousse [a], J. Hoszowska [a], A. Kubala-Kukuś [c], M. Pajek [c]

[a] Department of Physics, University of Fribourg, 1700 Fribourg, Switzerland
[b] Paul Scherrer Institut, 5232 Villigen-PSI, Switzerland
[c] Institute of Physics, Jan Kochanowski University, 25-406 Kielce, Poland
[d] Department of Physics, University of Oulu, 90014 Oulu, Finland

The grazing emission X-ray fluorescence (GEXRF) technique was applied to the analysis of different Al films, with nominal thicknesses in the range of 1 nm to 150 nm, on Si wafers. In GEXRF the sample volume from which the fluorescence intensity is detected is restricted to a near-surface region whose thickness can be tuned by varying the observation angle. This is possible because of the refraction of the fluorescence X-rays and the quite long emission paths within the probed sample. By recording the X-ray fluorescence signal for different shallow emission angles, defined relatively to the flat, smooth sample surface, the deposited Al surface layers of the different samples could be well characterized in terms of layer thickness, layer density, oxidation and surface roughness. The advantages offered by synchrotron radiation and the employed wavelength-dispersive detection setup were profited from. The GEXRF results retrieved were confirmed by complementary measurements. The experimental setup, the principles and advantages of GEXRF and the analysis of the recorded angular intensity profiles will be discussed in details.

http://doc.rero.ch

1. Introduction

Thin film depositions or coatings can be prepared by different methods like atomic layer deposition (ALD) [1], chemical vapor deposition (CVD) [2], molecular beam epitaxy (MBE) [3], magnetron sputtering [4], pulsed laser deposition (PLD) [5], spin coating [6] or electrospraying [7]. They are important for both technological and scientific applications. The aim of the layer deposition is to modify the thermal, mechanical, optical, chemical or electrical properties of a system. Examples of applications are organic surface modification, chemical sensors, photoelectrochemical cells, photocatalysis, structured semiconductor applications, mass storage and microelectronic devices (metal-oxide-semiconductors, dynamic random access memory), laser and X-ray optics (lenses, mirrors and multilayers). Technological progresses in the microelectronic and the solar cell industries with the inherent device size downscaling result in more demanding requirements for the thin film production and analysis. A better characterization is also asked for novel materials with high dielectric constants and oxynitride layers, which are both foreseen to replace silicon dioxide

* Corresponding author at: Paul Scherrer Institut, 5232 Villigen-PSI, Switzerland. Tel.: +41 56 310 3555.
E-mail address: yves.kayser@psi.ch (Y. Kayser).

http://doc.rero.ch

because of diffusion problems and defect density, polymer films and very thin films in the nanometer range.

As a specific example of thin-film applications, Al depositions on Si were used during some decades in the microelectronic industry, for example in the production of integrated circuits. However, the advances in the performance of semiconductor devices and their increased complexity revealed some limitations in the use of Al so that alternatives were looked for (Ag and Cu mainly) [8] although applications with Al are still realized [9]. The better adhesion of Al to the Si surface and the low intermiscibility of Al (resp. aluminates of a metal) and Si, are reasons why Al depositions on Si are still used, e.g., as a buffer layer, a diffusion barrier or an interconnect material, to circumvent the disadvantages of other metals [10,11]. In the self-encapsulation technique [12,13] the migration of Al through the superposed layer towards the surface and the subsequent oxidation to wear-resistant Al_2O_3 allows to use the deposited Al also for the formation of a passivating layer which prevents corrosion. To take advantage of this property, Al layers can also be oxidized, the native oxide layer being usually too thin [14,15]. Examples of Al depositions with different thicknesses on the top of Si by different techniques and the subsequent study of the Al layer regarding some of its properties can be found in [16–21]. The control and characterization of the film and also the interface quality with respect to the composition, oxidation, diffusion, density, thickness and roughness are necessary in order to properly tailor nanoscaled devices regarding the surface topography and physical properties. A better knowledge of the dependence of these properties on the process parameters can thus help to select and optimize the thin film preparation and deposition process.

To analyze thin layers deposited on a substrate, different techniques can be used, each of them having its merits and inherent limitations in terms of sample consumption, cost of analysis, quantification, chemical and elemental sensitivity, lateral and depth resolution, and accessible depth region. In secondary ion mass spectroscopy (SIMS) [22], respectively time-of-flight (TOF) SIMS [23], the depth composition of the sample is derived from the sputter rate. It is a very precise, quantitative analytical technique which offers an excellent lateral resolution [24] but requires an ultra-high-vacuum (UHV) setup and suffers from the formation of a transient region making a reliable characterization of the first few nanometers impossible until an equilibrium regime between the implanted and sputtered ion yields is established. Thus, SIMS cannot be used to characterize very thin films or changes in the chemical composition at the surface, e.g., oxidation of the surface layer. Rutherford backscattering (RBS) [25] and medium energy ion scattering (MEIS) [26], the related technique, are in contrast to SIMS non-destructive techniques, thus no changes in the sample properties are to be expected, but have drawbacks regarding the achievable depth and lateral resolution, the efficiency for light elements and the mass resolution for heavy elements. Also an independent determination of the density and the thickness is not possible. Techniques based on electrons [27] like Auger electron spectroscopy (AES) or X-ray photoelectron spectroscopy (XPS) are surface-sensitive and give, in contrast to ellipsometry [28], scanning electron microscopy (SEM) [29] or scanning tunneling microscopy (STM) [30], a direct information on the elemental and chemical composition. However, the mean penetration range of electrons severely limits the thickness of the sample which can be analyzed if this technique is not combined with sputtering. In the latter case, the analysis implies sample consumption and that reference samples are necessary for a proper calibration of the depth scale since the sputter rate varies with the chemical composition. Furthermore, absolute quantitative measurements are difficult to realize if not impossible. Particle induced X-ray emission (PIXE) based depth-profiling is characterized by a poor depth-resolution and can only be successfully applied to study some specific samples [31]. A comprehensive comparison of different analytical techniques for surface analysis is given in [32], further comparisons of surface-sensitive techniques can be found in [33–36]. Often a combination of the different techniques is necessary to gather the required information.

With respect to the mentioned techniques, methods based on X-rays like diffraction, scattering or, as in the present study, X-ray fluorescence (XRF) are competitive in terms of characterization of the surface [37]. They are in addition non-consumptive and do not necessarily require a high-vacuum environment like particle-based methods. At the same time they require little or no sample preparation, can be applied to a wide range of materials regarding the elemental and chemical composition as well as the concentration, allow for quantitative measurements and are characterized by a high surface-sensitivity if combined with a grazing incidence or emission geometry. Usually the efficiency of surface analysis (or interface analysis in the case of multilayered samples) by means of X-ray probing is limited by the weaker interaction of X-ray photons with matter as compared to ions and the inherent rather large penetration depth of the incident primary X-rays into the sample. In grazing incidence XRF (GIXRF) and grazing emission XRF (GEXRF) the capability to analyze the surface is improved by varying the incidence angle, respectively the exit angle, around the critical angle for total external reflection, which depends on the material and the wavelength of either the incident or the fluorescence X-rays, and by monitoring the fluorescence intensity (Fig. 1). The probed depth region, which depends on the angle, varies in this angular range from a few nanometers to several hundred nanometers (see Fig. 3 for the case of Al and the Al Kα line in GEXRF conditions). Consequently, because of the wide range of accessible depth regions, GIXRF and GEXRF have, compared to SIMS, AES, or XPS, less restrictions regarding the film thickness that can be analyzed. Moreover, depending on the layer thickness, the number of deposited atoms can differ by several orders of magnitude, but the linearity in the intensity response of X-ray detectors provides enough flexibility for quantitative measurements. As discussed in this paper both, GIXRF and GEXRF, have been used for thin film analysis. Other application domains are micro- and trace analyses, surface contamination control (see [38–41] for GIXRF and [42–44] for GEXRF among others for semiconductor applications) and depth-profiling of ion-implanted samples (see for example [45–47] for GIXRF and GEXRF, respectively). In the latter application a comparison of GIXRF and GEXRF for Al implantations in Si can be found in [48]. In the two former application domains the X-ray fluorescence intensity is detected at a fixed incidence or emission angle below the critical angle since the primary goal is to detect the presence of contaminants. In this case the grazing incidence geometry is commonly referred to as the total reflection of X-ray fluorescence (TXRF) technique [49–51]. TXRF has also been combined with sputter etching [52] to realize depth-profiling experiments. A comparison of GEXRF with TXRF and other X-ray emission techniques in the domain of trace element analysis can be found in [53]. In this article the investigation of thin films regarding the thickness, roughness, density and oxidation level by means of synchrotron radiation based high-energy-resolution GEXRF will be reported for the example of Al deposited on Si wafers with different nominal thicknesses (assuming continuous layers).

2. GIXRF and GEXRF

From an experimental point of view, GEXRF and GIXRF are based on the refraction of the incident respectively emitted X-rays at the flat, smooth sample surfaces or intra-sample interfaces in order to enhance the sensitivity towards the surface and near-surface regions

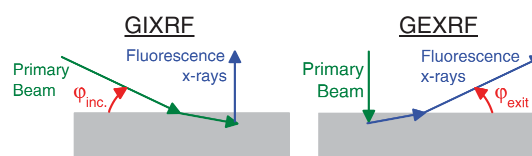

Fig. 1. Basic concept for a GIXRF (left) and a GEXRF (right) experimental setup.

with respect to the bulk sample. Indeed for X-rays the real part of the complex refractive index n (related to the scattering properties) of solid samples is smaller than one by a decrement factor of 10^{-3}–10^{-6}. Consequently, X-rays undergo total external reflection at the sample surface at small enough incidence angles. A second factor contributing besides the refraction to the surface-sensitivity are the implicit long incidence paths, respectively emission paths, within the sample. The consequences are a larger sensitivity to the sample matrix and a limited depth region effectively contributing to the detected X-ray fluorescence yield because of absorption (related to the complex part of n). The basic idea of the grazing geometries is to either enhance the excitation process of the surface and/or near-surface region with respect to the bulk volume (GIXRF) or to restrain the region from which the excited fluorescence signal can be detected to the surface and/or near-surface region (GEXRF).

The grazing emission geometry was derived in 1983 from the grazing incidence geometry [54]. In GIXRF, and also in the X-ray standing wave (XSW) technique under total reflection conditions [55], an X-ray standing wave-pattern is created by the coherent superposition of the incident and reflected wave for incidence angles below the critical angle of total external reflection. For thin layered samples, depending on the incidence angle and the different refractive indexes, the X-ray standing wave-pattern is created on the top of the surface or within the thin layer. In the first case the incidence angle has to be below the critical angle for the surface layer, in the latter case between the critical angles for the surface layer and the bulk, the necessary condition being that the critical angle for the bulk is larger. A restriction for XSW is that the period of the standing wave-pattern should not be much larger than the layer thickness. The wave-pattern is characterized by planes with constructive and destructive interferences which are parallel to the sample surface and whose position with respect to the reflecting surface and periodicity depend on the incidence angle and the incident wavelength. Only an evanescent, exponentially damped wave, propagating along the surface penetrates into the sample region below the interface on which the standing wave-pattern is created (typically 3–5 nm). Thus, there is a non-negligible chance for the absorption of incident X-rays and the emission of fluorescence radiation in the mentioned sample region. The short vertical penetration range is due to the energy and momentum conservation. By varying the incidence angle, the evanescent wave is modified due to the varying penetration depth (kinematical factor) and the changing standing wave-pattern (dynamical factor) [54]. For continuity reasons the intensity of the evanescent wave has to be equal to the one of the standing wave at the reflecting interface. The total external reflection of X-rays not only improves the excitation efficiency for fluorescence radiation in the near-surface or -interface region but also prevents in addition fluorescence excitation in the bulk. For larger incidence angles the reflection coefficient drops towards zero and the depth region contributing to the measured X-ray fluorescence intensity starts to increase since the incident beam penetrates into the sample volume below the reflecting interface. However, upon the transition through the separating interface the incident beam is deviated because of the refraction process. Also, due to the shallow incidence angles, the X-ray absorption is quite pronounced in the depth direction, limiting the volume in which X-ray fluorescence is effectively excited. Depth-sensitive measurements of multilayers and thin films deposited on a surface were performed by means of GIXRF [56–60] or by means of XSW under grazing incidence conditions [55,61]. The thickness and the density of the films as well as the elemental amount or quantity of deposited material were assessed. In most cases the assumption of a stratified model with homogeneous and discrete layers was made to fit the data by inverse modeling, the initial model needing to describe the probed sample already well enough for a reliable interpretation [55,57]. Also the surface roughness had to be considered [62,63] and the X-ray source coherence lengths were found to have a major impact on the extension of the standing wave-pattern [49,50]. A different grazing incidence technique is X-ray reflectometry (XRR) [64]. In XRR the change in the reflected intensity is monitored as a dependence of the incidence angle in order to deduce the layer density (from the critical angle) as well as the layer thickness and interface roughness (from the Kissing fringes in the intensity curve) [65–68]. From an experimental point of view, the studied layer is required to have a sufficient thickness and to be laterally homogeneous to be suitable for XRR measurements.

With respect to GIXRF, GEXRF can be considered as being based on an inverted setup in the sense that the paths for excitation and detection of the X-ray fluorescence intensity are exchanged in order to switch from an angle-dependent excitation of the X-ray fluorescence under grazing incidence conditions to an angle-dependent detection under grazing emission conditions (Fig. 1). Actually, the GIXRF and GEXRF setups are not only similar but, because of the principle of microscopic reversibility and reciprocity [69], also equivalent from a physical point of view: if grazing incidence and grazing emission experiments were performed with the same wavelength λ, the distributions of the atoms contributing to the observed fluorescence yields would be identical [54].

In GEXRF, the primary beam penetrates into the bulk sample and, thus, no standing X-ray wave-pattern is created. However, for sufficiently small observation angles relatively to the sample surface only the X-ray fluorescence emitted by surface-near atoms is observable. Indeed, X-rays emitted from atoms located far from the surface interface are refracted away from the surface upon the transition of this interface (inverted path with respect to the incidence X-rays in GIXRF). Consequently for observation angles in the range from 0 mrad to the critical angle only the fluorescence emitted by near-surface atoms can be detected. GEXRF is characterized by the excitation of an internal evanescent wave, equivalently to the evanescent wave in GIXRF. This results in a considerably enhanced surface sensitivity as the contribution of the bulk atoms to the detected intensity is suppressed and explains, thus, the surface-sensitive character of GEXRF. For observation angles above the critical angle, the fluorescence signal produced further away from the sample surface is also observable. Nevertheless, the probed depth region is still on the submicrometer scale since the shallow observation angles result in long emission paths within the sample and consequently in a quite pronounced absorption. As mentioned, GEXRF was also used, like GIXRF, for thin-film and layer analysis of metallic elements or alloys [70–74] in order to study surface oxidation, growth processes, the influence of neighboring low-Z layers or simply the density and thickness of the deposited films. The GEXRF method shows, thus, a good potential for layer characterization and for process control, since besides the elemental information also structural information on the thin films can be obtained. The explanation for the enhanced sensitivity of GEXRF for these sample types is given by the fact that, as long as the reflection coefficients on the different interfaces are non-zero, there is more than one possible emission direction towards the detector (Fig. 2). Depending on the differences in the path lengths towards the detector, constructive or destructive interferences occur for sources at different well-defined vertical positions. This is the same condition as the one for the creation of a standing wave-pattern inside a thin film or layer in grazing incidence conditions except that in grazing emission the position and periodicity of the planes depend on the emission angle and the fluorescence wavelength. However, only for paths with no (directly transmitted X-rays) or an even number of reflections on the interfaces is the difference in the path length independent from the vertical position of the source and interference fringes are observable in the angular profile. The oscillations observed in the angular intensity profile of the Cr Kα line of Cr/Au/Cr layers deposited on quartz glass were interpreted as an experimental evidence of the aforementioned reciprocity theorem [75]. The interference pattern is usually more pronounced if the refractive index of the substrate is smaller than the refractive index of the

http://doc.rero.ch

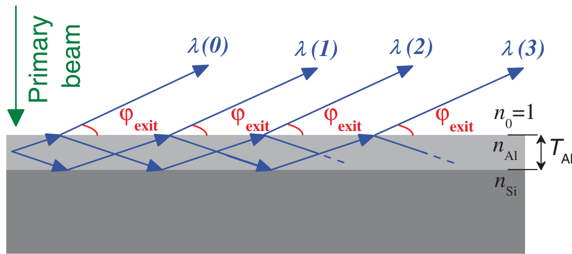

Fig. 2. Illustration of the different possible emission paths of fluorescence X-rays (wavelength λ) from an Al-layered Si wafer for a fixed observation angle φ_{exit} close to the critical angle. The number in parentheses indicates the number of reflections undergone for each path, the probability that a fluorescence photon follows a given path depends on the reflection (and thus transmission) factor for the considered exit angle. Note that only those paths corresponding to an even number of reflections give rise to constructive interferences that depend solely on the exit angle and not on the depth position of the fluorescence sources.

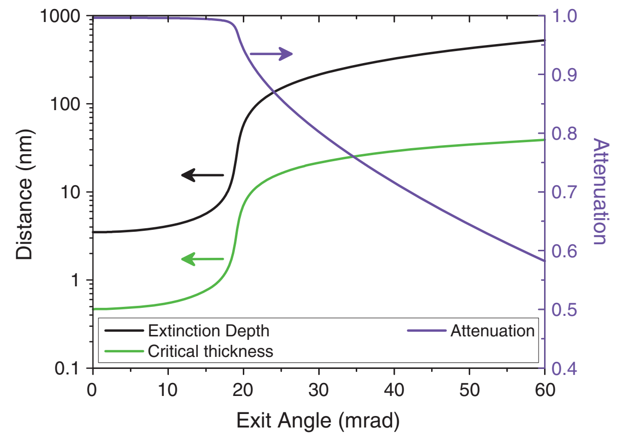

Fig. 3. Variation with the exit angle of the extinction depth and of the critical thickness for Al and the Al Kα fluorescence line. The attenuation in Al of the primary X-ray beam ($E_{0,Al}$ = 1.582 keV, normal incidence) within the extinction depth of Al Kα is also shown. The extinction depth stands for the depth from which the emitted fluorescence intensity is attenuated by a factor e^{-1} within the sample, while the critical thickness indicates up to which depth absorption effects can be safely neglected.

layer and consequently the dependence of the angular profile on the thickness will be more distinct. The latter condition is of prime importance for trace element analysis. For Al layers deposited on Si this is, however, not the case. It will be shown in this article that an accurate analysis was nevertheless possible.

From an experimental point of view one should note that the critical angle referred to in GEXRF is larger than in GIXRF since it is defined relatively to the wavelength of the fluorescence X-rays and not to the one of the primary X-rays. This mainly results in a rescaled angular range with respect to the critical angle. Also due to the different X-ray energies of interest, once below (GEXRF), once above (GIXRF) the absorption edge, the sensitivity towards the sample matrix is different. The most crucial difference concerns, however, the incident radiation used to excite the fluorescence radiation. For geometrical reasons, the surface region over which the standing wave-pattern extends varies inversely with the incidence angle. Thus, in GIXRF the beam spreads over a wide sample surface and laterally resolved studies with a resolution in the scale of a few micrometers are hardly feasible. In contrast to GIXRF, the grazing emission geometry is in combination with micro-XRF sources favorable for mapping applications. Such GEXRF mapping measurements were performed using a micro-sized collimated synchrotron radiation beam [42] or employing a polycapillary optics mounted in front of an X-ray tube [76–78]. Also, GEXRF setups can be combined with different excitation sources (protons [79], electrons [80], mono- or polychromatic X-ray beams) since the angular intensity dependence is essentially given by the refraction of the produced fluorescence X-rays. The advantage of using charged particles is that the fluorescence signal is mainly produced close to the surface, i.e., in the region of interest to which the GEXRF measurement is sensitive, due to the lower penetration depth of particles. The disadvantage is, however, a more complicated analysis since the production of the fluorescence signal in the analyzed sample region (Fig. 3) cannot be assumed to be depth-independent. In Fig. 3, the attenuation of the primary X-ray beam for the extinction depth corresponding to the exit angle is shown. The extinction depth corresponds to the depth from which the emitted fluorescence intensity is attenuated by a factor of e^{-1} on the way from the fluorescence atom to the surface, whereas the critical thickness corresponds to the depth region for which absorption effects for the incident and emitted radiation can be safely neglected [81]. This restriction for the linear regime of calibration curves was first discussed for TXRF [82].

On the other side, GIXRF setups are characterized by a quite large solid angle because the energy-dispersive detectors are mounted close to the target surface, whereas the unavoidable collimation of the fluorescence radiation, needed to define the observation angle, reduces the luminosity of GEXRF setups. However, this allows for the use of wavelength-dispersive setups, where a collimation of the fluorescence radiation is automatically realized via the Bragg condition. The drawback related to the small solid angle characteristic for wavelength-dispersive instruments is in addition partly canceled by the fact that no additional collimator is needed. The main advantages offered by wavelength-dispersive setups are their energy resolution, providing a greater sensitivity to chemical states and a good separation of the many L-lines of mid-Z elements and/or M-lines of heavy elements, their good background rejection capabilities, which contributes to an improved signal-to-background ratio, and finally their sensitivity towards low-Z elements. These advantages compensate partially the lower luminosity. As explained in the next section this proved, in combination with the advantages offered by synchrotron radiation (high flux and energy-tunable, monochromatic X-ray beam) to be extremely useful for the characterization of Al films on Si.

For the sake of completeness it should be mentioned that the combination of grazing incidence and grazing emission geometries was also realized for thin film analysis [83,84], the chemical conditions and surface/interface roughness between two layers being analyzed together with the film density and thickness. Either the dependence of the X-ray fluorescence intensity on the incidence angle was measured for different emission angles or vice-versa which offers the possibility to acquire different data sets for one sample. Due to the collimation of the incident and emitted X-ray radiation, the detection efficiency of these setups is reduced. The main motivation for this type of setup is the very low background since the excitation and the detection process focus both on the near-surface regions. Finally, combinations of other X-ray analytical techniques like absorption (with grazing incidence [85–87] and grazing emission [76,88,89]) and diffraction (with grazing incidence [90,91] and grazing emission [92]) were also realized to determine the nearest-neighbor configurations or the surface structure.

3. Experimental

The presented GEXRF measurements were realized at the ID21 beamline of the European Synchrotron Radiation Facility (ESRF) in Grenoble, France. The high-resolution reflection-type von Hamos curved crystal X-ray spectrometer of the University of Fribourg [93] was installed downstream of the beamline's scanning X-ray microscope (SXM) chamber. The University of Fribourg's von Hamos spectrometer, when installed at the ESRF ID21 beamline and configured in the GEXRF geometry, has been characterized in terms of detection limits [42,43] and depth-profiling capabilities [47,48]. The main components of the spectrometer (Fig. 4) are a cylindrically curved crystal and a position sensitive detector. The detector was a two-dimensional back-illuminated coupled charge device (CCD) which has been

http://doc.rero.ch

characterized in [94]. It is placed on the curvature axis of the crystal, consists of 1340 × 400 pixels ($h \times v$), each pixel having a size of 20 × 20 μm^2 and the electronic's read-out speed is 1 MHz. The bending of the crystal offers a focusing on the CCD in the non-dispersive plane and thus an enhancement of the collection efficiency whereas the positional information stored by the CCD allows for a discretization of the covered Bragg angle range along the dispersive axis. The crystal and detector positions are fixed by the lattice constant of the employed crystal and the measured fluorescence energy via the Bragg law. Since the Bragg law fixes the detection path from the sample towards the detector, grazing emission conditions are realized by tilting the flat, smooth target surface close enough to the detection direction. For the detection of the Al Kα, respectively Si Kα fluorescence lines, the spectrometer was equipped with the ADP (101) crystal ($2d$ = 10.642 Å, curvature radius R =254 mm, crystal height h = 100 mm). Only events diffracted by the crystal are incident on the CCD, background events being mainly due to the electronic noise, scattering and cosmic events. Their contribution to the measurement is reduced by the subtraction of a background image to each acquired frame and an energy discrimination in the analysis of the detected events.

The primary X-ray beam, which enters the spectrometer chamber parallel to and at the height of the spectrometer's dispersion plane, was delivered by a wiggler and monochromatized by two Ni/B_4C multilayers. Higher-order harmonics were rejected by means of two Si mirrors tilted at an angle of 12 mrad with respect to the incident primary beam. The beam size was defined by a pinhole with a diameter of 1 mm. The beam energy resolution was about 6 eV for the two selected primary X-ray beam energies, namely $E_{0,\mathrm{Al}}$ = 1.582 keV for the detection of the Al-Kα line and $E_{0,\mathrm{Si}}$ = 2.000 keV for the Si-Kα line, both energies being just above the K-absorption edge of the respective element. The primary beam photon flux was about 5 × 10^{10}, respectively 2 × 10^{11} photons per second for the mentioned energies. The choice of the excitation energy for the Al Kα fluorescence line was guided by several considerations. At the excitation energy of 1.582 keV, in addition to the suppression of the strong Si Kα fluorescence line and the photoelectric absorption cross-section of the Al K-shell being close to its maximal value, a considerable background reduction was achieved. Indeed, a possible overlap of the K X-ray resonant Raman scattering (RRS) of the Si L-shell [95], whose cut-off energy depends on the primary beam energy, with the Al Kα fluorescence line was avoided while the elastic peak was still not incident on the CCD [42,43]. Note that this separation could only be achieved thanks to the high energy resolution of the von Hamos spectrometer. Indeed, with an energy-dispersive setup the Al Kα fluorescence line could not be separated from the Si RRS-KL and the elastic signal even with the best available detectors in terms of energy resolution. The remaining background overlapping with the Al Kα line was found to arise only from the weak Si RRS-KM and the intrinsic noise of the CCD detector (about 2.5 × 10^{-4} counts per second), which allowed for a direct detection limit of 3.7 × 10^{12} atoms/cm^2 for Al impurities on the surface of Si wafers [43]. The background conditions for the measurements with the Al-layered samples are illustrated in Fig. 4. The combined advantages of the energy-tunability of synchrotron radiation beams and the high energy resolution detection are highly valuable if the fluorescence line of a trace element in or on a bulk sample with an atomic number higher by one unity has to be detected [96].

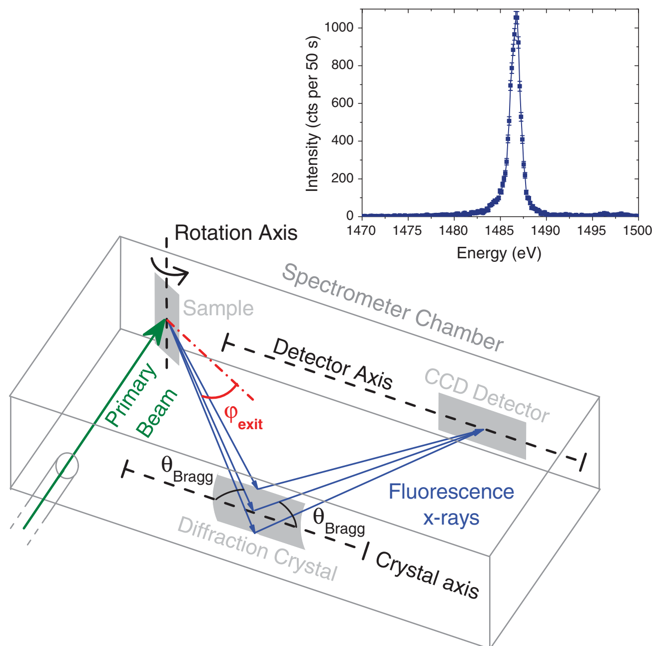

Fig. 4. Schematic drawing of the experimental setup (details in the text) and experimental spectrum of the Al-Kα intensity acquired for the 10 nm Al-layered Si sample at an exit angle of 40 mrad, illustrating the excellent background conditions achieved in the experiment. The experimental spectrum corresponds to the projection onto the dispersion axis of the spectrometer of the CCD events sorted previously by an energy discrimination.

For each fluorescence line, the grazing exit angle is defined with respect to the corresponding Bragg angle. However, for a fixed target angular position the exit angle varies on the CCD along the dispersion direction, i.e., the detector axis, as a function of the Bragg angle. This contributes, together with the Darwin width of the crystal and the natural linewidth of the fluorescence signal, to the angular resolution of the grazing emission experiment, even if this contribution is attenuated by the intensity distribution of the measured fluorescence X-ray line. In order to acquire grazing emission intensity profiles with a proper angular resolution an area of interest is defined on the CCD in both the horizontal and vertical directions. Only X-rays detected within the area of interest are taken into account in the angular intensity profile. In the selection of the area of interest on the CCD a compromise between intensity and angular resolution has to be made. Horizontally the region of interest is centered on the maximum peak intensity of the measured X-ray fluorescence line (inset of Fig. 4), vertically it is centered on the dispersion plane which is defined by the crystal and detector axes and which contains the incident synchrotron beam. The vertical restriction is necessary because of geometrical considerations due to the vertical extension of the irradiated sample area and the cylindrically curved diffraction crystal. The fluorescence signal from a source atom which is vertically off-axis with respect to the dispersion plane will be reflected by the crystal to a CCD region which is vertically and horizontally displaced with respect to the signal from a fluorescence source which is on-axis. Thus, the exit angle at which the fluorescence radiation left the sample changes along a vertical line of the CCD. A last contribution to the angular resolution arises from the fact that the exit angle of the fluorescence radiation emitted by a single source and which is incident on the crystal planes at the Bragg angle is not constant but varies along the crystal height. This is imposed by the spectrometer geometry and the condition to realize grazing emission conditions. Indeed, to realize GEXRF experiments, the sample surface cannot be oriented vertically to the dispersion axis. The blurring of the angular resolution depends in principle on the crystal height and the radius of curvature. The effect of this contribution is, however, less important when a region of interest is defined on the CCD and either the sample or the CCD is out of the crystal's focus, i.e., not positioned on the axis of curvature of the crystal. In the present case the spectrometer design foresees an off-axis sample positioning [93].

The horizontal extension of the irradiated sample area W_{Beam} does not contribute significantly to the angular resolution. In grazing emission conditions the crystal sees the target as a line-like source, the contribution to the angular resolution is then proportional to $W_{\mathrm{Beam}} \times sin\varphi$ where φ stands for the exit angle. The proportionality factor is given by the spectrometer geometry. Consequently, the spectrometer can be operated in a slit-less mode without deteriorating the angular resolution,

http://doc.rero.ch

http://doc.rero.ch

the contribution of the diffracting crystal being the Darwin width. The slit-less operation mode presents the advantages that no beam profile effects have to be considered and that the luminosity of the setup is slightly increased since, horizontally, the whole irradiated surface of the sample contributes to the measured fluorescence. The experimental angular resolution of the presented setup was assessed by a convolution of the angular profile which best fitted the experimental data with a Gaussian, the width of the Gaussian being the intrinsic instrumental angular broadening. The resolution was found to be 0.17 mrad. This is better or comparable to the reported angular resolutions of other GEXRF setups which are of the order of 1 mrad or lower [49,74,76]. In the latter setups either an analyzer crystal or an energy-dispersive detector in combination with a collimator slit system was employed to define the grazing emission angle. A compromise between angular resolution and detection sensitivity had to be made depending on the main experimental purposes (trace-element control or structural surface characterization).

The intensity of the Al Kα-line was measured at 100 different angular positions separated each by 0.4 mrad and acquisition times of 50–200 s for each step, depending on the sample. The Si Kα fluorescence X-ray line was measured at 40 different points separated by 1 mrad with a collecting time of 20–30 s per point. The accuracy of the system used to orientate the sample is 0.04 mrad. During the acquisition of an angular profile, all experimental parameters (crystal reflectivity, solid angle, CCD efficiency) remained unchanged. The angular profiles for Si were needed for calibration purposes in order to associate to the different angular positions of each sample the corresponding emission angles. Indeed, the exit angle can be controlled only on a relative scale and in order to know the exit angle on an absolute scale, a reference position is needed. In our case this reference position corresponds to the critical angle $\varphi_{c,\mathrm{Si}}$ of the Si Kα-line. The corresponding sample position is extracted from a Gaussian fit of the derivative of the measured angular intensity curve for the Si Kα-line. Once this reference position is known, the offset of the angular scale and consequently the absolute exit angle can be determined for each position of the investigated sample. For sufficiently thin-layered samples, the critical angle is supposed to correspond to the one of a Si pure bulk. With increasing thicknesses, the influence of the layer above the bulk needs to be accounted for as the experimentally determined critical angle is shifted with respect to the bulk value (see Fig. 5, upper right panel). Depending on the ratio of the refractive indexes for the layer and the bulk material for the fluorescence line emitted from the bulk, the influence of the layer results either in a strong damping of the fluorescence line or in a shift of the critical angle in the angular intensity profile as it is the case for the Al-layered Si wafers.

The studied Al-layered Si samples were produced for nominal Al layer thicknesses of 1, 5, 10, 20, 30, 50, 74, 130 and 150 nm. The silicon wafers were produced at the Institute of Electronic Materials Technology (ITME), Warsaw, Poland, by the Czochralsky method and were cut and polished. The Al layers were then deposited by sputtering with an electron gun and the deposited mass of Al (supposed to be directly proportional to the layer thickness) was monitored by a quartz micro-balance. In addition a 28 nm Al_2O_3-layered Si sample produced by MBE was analyzed.

4. Analysis methodology

The calculation of the angular dependence of an X-ray fluorescence line on the emission angle can be realized by means of the reciprocity theorem to derive the angular profile from GIXRF calculations [97] or by starting from a matrix formalism to simulate the propagation of an electromagnetic wave through a stratified medium [98,99]. In inverse modeling or forward calculation approaches, which are commonly used for measurements in grazing incidence, the disturbed X-ray wave-pattern has to be accounted for: in an iterative procedure, a model for the (a priori unknown) sample has to be assumed in order to calculate a standing wave-pattern [100] which allows to reproduce the experimental data, then the model is optimized. Alternatively, the GEXRF angular intensity profile can be calculated by considering directly the radiating X-ray fluorescence sources distributed in the sample and summing for each emission angle their individual contributions to the detected X-ray fluorescence intensity [69,101]. This approach facilitates the interpretation since physical phenomena influencing the X-ray fluorescence intensity are directly taken into account and explicit analytic expressions for the angular intensity profile are obtained. The latter aspect is especially advantageous for the interpretation of experimental data since unknown parameters can be inserted as fitting parameters. With respect to a stratified media approach, where a stack of layers is used to characterize the deposited film, the number of calculation steps and free fitting parameters is considerably reduced. The analytic expressions from [69,101] for a thin film sample and the bulk below will be reproduced hereafter. They allow to directly fit the experimental data. For a thin Al layer on the top of a bulk Si substrate the change of the fluorescence intensity I with the grazing emission angle φ can be calculated as follows

$$\begin{aligned} I(\varphi) = {} & |t_{\mathrm{Al}\nearrow\mathrm{vac.}}|^2 \\ & \times \frac{1-e^{-(2\mathrm{Im}(k_{\mathrm{Al}})+\mu_{\mathrm{Al}}(E_{0,\mathrm{Al}})\rho_{\mathrm{Al}})T_{\mathrm{Al}}}}{2\mathrm{Im}(k_{\mathrm{Al}})+\mu_{\mathrm{Al}}\left(E_{0,\mathrm{Al}}\right)\rho_{\mathrm{Al}}} \\ & \times \frac{1+|r_{\mathrm{Al}\searrow\mathrm{Si}}|^2 e^{-2\mathrm{Im}(k_{\mathrm{Al}})T_{\mathrm{Al}}}+\Psi(\varphi)}{\left|1-r_{\mathrm{Al}\nearrow\mathrm{vac.}}r_{\mathrm{Al}\searrow\mathrm{Si}}e^{-2ik_{\mathrm{Al}}T_{\mathrm{Al}}}\right|^2}, \end{aligned} \tag{1}$$

where the first factor corresponds to the change in the field strength of the fluorescence radiation upon transmission through the Al–vacuum interface,[1] the second factor corresponds to the average absorption of the synchrotron beam and intensity loss of the fluorescence radiation within the Al layer and the third factor corresponds to the interferences between fluorescence paths with different numbers of reflections on the Al–vacuum and Al–Si interfaces ($\Psi(\varphi)$ corresponds to a correction term). The transmission and reflection coefficients on the different interfaces are defined as follows:

$$t_{\mathrm{Al}\nearrow\mathrm{vac.}} = \frac{k_{\mathrm{vac.}}}{k_{\mathrm{Al}}}\frac{\sqrt{n_{\mathrm{Al}}^2-\cos^2\varphi}}{\sin\varphi+\sqrt{n_{\mathrm{Al}}^2-\cos^2\varphi}},$$

$$r_{\mathrm{Al}\nearrow\mathrm{vac.}}, = \frac{\sqrt{n_{\mathrm{Al}}^2-\cos^2\varphi}-\sin\varphi}{\sqrt{n_{\mathrm{Al}}^2-\cos^2\varphi}+\sin\varphi}$$

$$r_{\mathrm{Al}\searrow\mathrm{Si}}, = \frac{\sqrt{n_{\mathrm{Al}}^2-\cos^2\varphi}-\sqrt{n_{\mathrm{Si}}^2-\cos^2\varphi}}{\sqrt{n_{\mathrm{Al}}^2-\cos^2\varphi}+\sqrt{n_{\mathrm{Si}}^2-\cos^2\varphi}}$$

$$\text{with } k_{\mathrm{vac.}} = \frac{2\pi}{\lambda}\sin\varphi$$

$$\text{and } k_{\mathrm{Al}} = \frac{2\pi}{\lambda}\sqrt{n_{\mathrm{Al}}^2-\cos^2\varphi},$$

where λ stands for the fluorescence wavelength, namely the one of the Al Kα line. Due to the choice of the synchrotron beam energy, secondary fluorescence effects, i.e., fluorescence produced by the characteristic emission lines of Si, do not need to be accounted for. Normalized theoretical angular profiles for a 50 nm Al layer on the top of Si are shown in Fig. 6 for the Al Kα and also for the Al Kβ fluorescence lines together with the three factors which influence the shape of the angular profiles.

[1] For the interface between two media, the first named medium indicates from which side the fluorescence radiation is incident on the interface.

http://doc.rero.ch

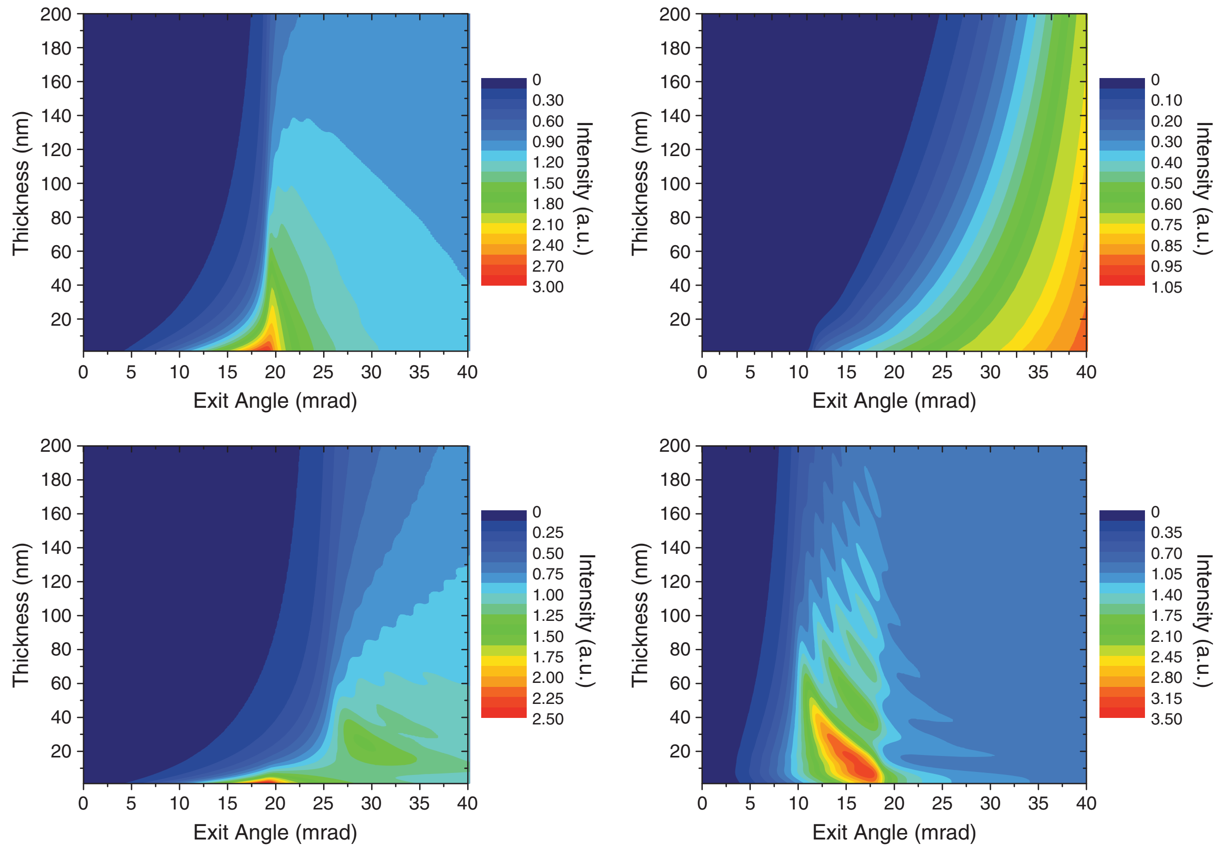

Fig. 5. Evolution of the grazing emission angular profile of Al-layered Si wafers for the Al Kα (upper left panel), Si Kα (upper right panel) and Al Kβ (lower right panel) fluorescence lines for different layer thicknesses. For a better comparison of the shapes of the angular profiles the angular profiles were normalized to an intensity of 1 at an exit angle of 60 mrad. In addition the Al Kα angular profile for Al_2O_3 on the top of Si was considered (lower left panel). A comparison with the pure Al layer shows a significantly different angular profile for an identical layer thickness, indicating that pure Al can be reliably distinguished from oxidized Al. In the Al Kβ angular profile more oscillations can be observed due to interferences since for this line the critical angle for Al is lower than for Si. The Si Kα angular profile is considerably attenuated with increasing Al layer thickness. For the largest layer thickness shown in the figure for the Al Kα of the Al-layered sample, the differences in the angular profile are less obvious, indicating a fundamental limit of the accuracy of the method for the thickness determination of the layers.

For the energy corresponding to the latter line the critical angle for Al is smaller than for Si. Therefore, interference effects are much more dominant in the shape of the angular intensity profile than for the Al Kα line. This can also be seen in Fig. 5 where the angular profiles for different layer thicknesses are calculated, the Al Kβ (lower right panel) angular profiles exhibiting more interference fringes than the AlKα (upper left panel) for an identical layer thickness.

The angular intensity profile for the Si Kα fluorescence line of the bulk Si wafer below the thin Al layer can be approximated by

$$I(\varphi)\approx|t_{Si\nearrow Al}t_{Al\nearrow vac.}|^2\times\; e^{-(2\mathrm{Im}(k_{Al})+\mu_{Al}(E_{0,Si})\rho_{Al})T_{Al}}\,\frac{1-e^{-(2\mathrm{Im}(k_{Si})+\mu_{Si}(E_{0,Si})\rho_{Si})T_{Si}}}{2\mathrm{Im}(k_{Si})+\mu_{Si}\left(E_{0,Si}\right)\rho_{Si}}\times\frac{1}{|1-r_{Al\nearrow vac.}r_{Al\searrow Si}e^{-2ik_{Al}T_{Al}}|^2},\qquad(2)$$

where

$$t_{Si\nearrow Al}=\frac{k_{Al}}{k_{Si}}\frac{2\sqrt{n_{Si}^2-\cos^2\varphi}}{\sqrt{n_{Al}^2-\cos^2\varphi}+\sqrt{n_{Si}^2-\cos^2\varphi}}$$

$$\text{with}\;\; k_{Si}=\frac{2\pi}{\lambda}\sqrt{n_{Si}^2-\cos^2\varphi}.$$

The physical interpretation of the three factors is the same as in the calculation of the thin film angular profile. Note that the complex refractive indexes n_{Al} and n_{Si} have to be changed to the ones corresponding to the Si Kα fluorescence wavelength. With respect to the thin film angular profile, the differences are the following. In the first factor the transmission of the Si Kα fluorescence radiation through the Si–Al interface and in the second factor the presence of the Al layer have to be considered while in the third factor only the interferences between fluorescence paths with zero or an even number of reflections on the Al–vacuum and Al–Si interfaces need to be calculated. Indeed there is no possible fluorescence path from the bulk with an odd number of reflections on the different interfaces.

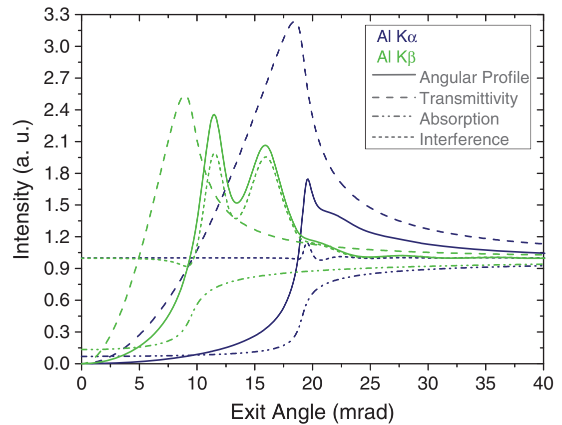

Fig. 6. Theoretical angular profiles calculated with Eq. (1) for the Al Kα and Al Kβ lines from a 50 nm Al-layered Si sample. The transmittivity, absorption and interference factors, i.e., the three factors present in Eq. (1) are also displayed for both profiles.

In Fig. 5 the theoretical angular profiles of the Al and Si Kα lines (upper left, resp. upper right panel) for ideal Al-layered Si samples with different layer thicknesses are represented. It can be seen that the features in the angular profiles depend pronouncedly on the layer thickness, showing that an accurate distinction between different Al-layered samples is possible.

In the abovementioned equations all the interfaces are considered, in the scale of the fluorescence wavelengths, to be ideally flat and smooth without any waviness or bending. While the Si wafer exhibits only a roughness in a sub-nanometer scale, the roughness of the deposited Al layers, however, cannot be assumed a priori to be negligible. The interface roughness can be included in the calculation by either modeling the thin layer as a multilayer stack with decreasing density, i.e., varying the index of refraction, towards the layer–vacuum interface or by taking a weighted linear combination of layers with different thicknesses. The characterization of an unknown sample where the roughness has to be extracted is, thus, not straightforward. For small roughnesses, a different approach consists in modifying the reflection and transmission coefficients to take into account the surface roughness, expressed as the root-mean square variation of the thickness [102]. Depending on the correlation length of the roughness, either the Debby–Waller/Rayleigh or the Névot–Croce approximation can be chosen. For the present samples, the latter approximation, which assumes a small correlation length, proved to be the most suitable to reproduce the experimental data while the roughness of the Si wafers could be safely neglected. This was checked for Si samples with and without an Al layer deposited on the top of the surface. The reflection and transmission factors for the Al–vacuum interface were therefore modified to

$$t_{\mathrm{Al}\nearrow\mathrm{vac.}} = t_{\mathrm{Al}\nearrow\mathrm{vac.}} * e^{-2k_{\mathrm{vac.}}k_{\mathrm{Al}}r_{\mathrm{Al}}^2}$$

$$\text{resp.}\ \ r_{\mathrm{Al}\nearrow\mathrm{vac.}} = r_{\mathrm{Al}\nearrow\mathrm{vac.}} * e^{(k_{\mathrm{vac.}}-k_{\mathrm{Al}})r_{\mathrm{Al}}^2}.$$

Results provided by the above relations are only approximately correct, some second order processes which are expected to influence the reflection and transmission coefficients being not accounted for [103].

The experimental angular profiles acquired using the previously presented setup were analyzed by means of Eqs. (1) and (2). The latter equation was used to calibrate the angular scale for each individual sample by assessing the offset with respect to the theoretical position. For this the presence of the Al layer had to be taken into account because of absorption in the Al layer and refraction at the Si–Al and Al–vacuum interfaces. Indeed, the absorption of the primary X-ray photons and of the fluorescence Si Kα X-rays, the energy of which just above the Al K edge, attenuates considerably the intensity in the bulk angular profile with increasing Al film thickness. In addition, since for the energy of the Si Kα X-rays the critical angle for Al is larger than the one for Si, the apparent critical angle in the angular profile for the Si bulk below an Al layer is shifted towards higher values with increasing Al layer thicknesses (Fig. 5, upper right panel). Both factors were accounted for by assuming an ideal Al layer, i.e., a layer with bulk density and no roughness, on the top of the bulk Si when fitting the Si Kα angular profiles. The calibration of the angular scale is crucial for a correct determination of the density and oxide concentration level in the Al layer. Indeed, for a fixed layer thickness, both factors influence the critical angle in the Al Kα angular profile whereas the roughness influences mainly the shape of the angular profiles. This can be observed in Fig. 7 where for a nominal layer thickness of 10 nm the influence of a varying oxide concentration (left panel), layer roughness (middle panel) or density (right panel) on the angular intensity profile are represented. Reversely, this emphasizes the importance of an accurate angular calibration of the experimental profiles in order to allow for a correct determination of the different physical properties.

The Al Kα angular profiles acquired from the different layers were fitted by means of Eq. (1) in order to extract the layer thickness, density, oxidation and surface roughness. The layer thickness extracted from the corresponding fit of the Si Kα bulk profile was used as an initial guess to estimate which values for the layer density, oxide concentration level and surface roughness give reasonable starting values for the fitting procedure. The density and the oxide concentration level were introduced into Eq. (1) through the complex refractive index,

$$\begin{aligned} n_{\mathrm{Al}} &= 1-\delta_{\mathrm{Al}} + i\beta_{\mathrm{Al}} \\ \rightarrow n_{\mathrm{Al}} &= c_{\mathrm{Al_2O_3}} * \left(1-d_\rho\delta_{\mathrm{Al_2O_3}} + id_\rho\beta_{\mathrm{Al_2O_3}}\right) \\ &\quad + \left(1-c_{\mathrm{Al_2O_3}}\right) * \left(1-d_\rho\delta_{\mathrm{Al}} + id_\rho\beta_{\mathrm{Al}}\right), \end{aligned} \tag{3}$$

where d_ρ represents the relative reduction in density with respect to the bulk density and $c_{\mathrm{Al_2O_3}}$ represents the oxide concentration relatively to pure Al. Indeed, the scattering and absorption parts of the complex refractive index depend linearly on the density, whereas the relative oxide concentration level $c_{\mathrm{Al_2O_3}}$ is extracted by assuming a linear combination of the refractive indexes of pure Al and Al_2O_3. The ratio between oxidized and not-oxidized Al is then directly obtained from the fit. The distinction between pure Al and Al_2O_3 was facilitated by the considerably different critical angles for the Al Kα fluorescence line (19.06 mrad for Al, 25.50 mrad for Al_2O_3). For an identical layer thickness, the angular profiles of Al and Al_2O_3 differ considerably because of the difference in the scattering part of the complex refractive index for the energy of the Al Kα line (Fig. 5, upper left and lower left panels). It was assumed that the relative reduction in density d_ρ with respect to the bulk values (2.7 g/cm^3 for Al and 3.97 g/cm^3 for Al_2O_3 and Fig. 7, left panel) was the same for pure Al and for Al_2O_3 since the oxidation only occurs after the deposition of the Al layers. If necessary, i.e., for high oxide concentration levels, the offset of the angular scale assessed from the Si Kα bulk angular profile was reevaluated. During the fitting procedure, the experimental angular profile was fitted repeatedly with only one of the four parameters being a free variable. First the layer thickness was fitted and the other three were kept fixed at a value which was considered a good starting point by a preliminary fit. For each new least-squares fit, defined as minimization of the sum of the squares of the residuals (the difference between each data point and its fitted value), the free variable was alternated in a fixed order and the fitting procedure was only stopped after all four fitting parameters converged to their final result. The order of the sequence in which the fitting parameters were alternated did not have a noticeable, i.e., larger than the fit error which was the standard error returned by the algorithm for each individual parameter, influence on the final result. The final results obtained for the layer thickness and density, the oxide concentration level and the layer surface roughness are displayed in Table 1. Examples of fitted experimental GEXRF profiles are displayed, together with the theoretical expectation, in Fig. 8. While the Al-layered Si samples are well fitted for the different examples which are displayed, the Al_2O_3 layered Si sample is less well fitted. A reason could be that the refractive index of Al_2O_3 grown by MBE is different than the one which was assumed, i.e. the one of natural Al_2O_3. This shows a limitation of the grazing XRF methods, the complex index of refraction for the material and energy of interest has to be well known. Complementary measurements to determine beforehand one of the different fitting parameters would help to solve such issues, e.g., XRR could be used to determine the exact value of the layer density.

In the fitting procedure, the algorithm allowed also for island-like features on the Si wafer surface in case of strongly dispersed lateral distributions for the thinnest Al films. For this the angular intensity profile for thin layers (Eq. (1)) was linearly combined with an equation

http://doc.rero.ch

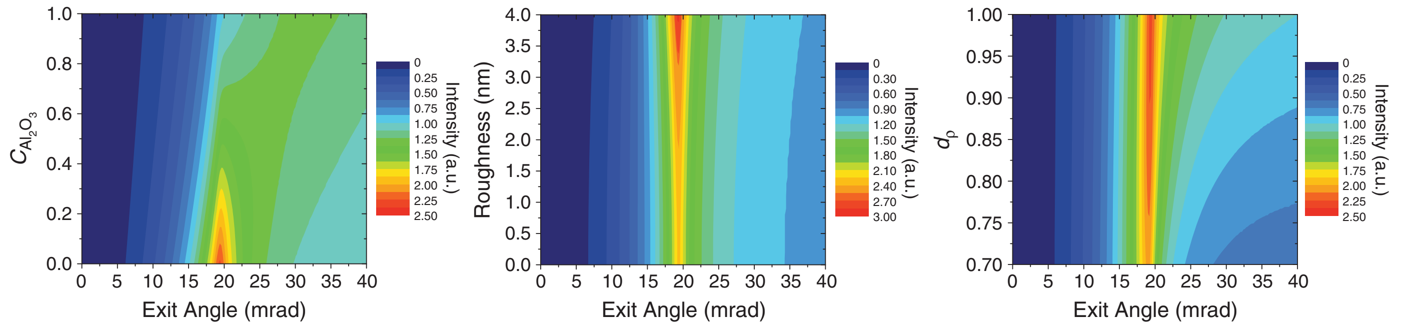

Fig. 7. Evolution of the grazing emission angular profile of Al-layers Si wafers for the Al Kα line of a 10 nm thick layer as a function of a varying relative oxide concentration (left panel), roughness (middle panel) or density (right panel). As in Fig. 5 the intensity was normalized to 1 at 60 mrad. The shape of the angular profiles changes quite pronouncedly with each of these parameters, indicating that the latter can be reliably extracted from the fits. For a varying relative oxide concentration or density the position of the maximum intensity position shifts towards larger, respectively smaller exit angles, while it does not shift with a varying roughness.

describing the angular fluorescence intensity profiles for particle-like distributions on the surface, the normalized linear combination factor representing the respective weight for each type of distribution. The theoretical angular intensity profile of a low-concentration particle distribution (particle height S) on the top of a sharp interface with the bulk is given by

$$I(\varphi)\approx\frac{1-\exp(-2\mathrm{Im}(k_{Al})S)}{2\mathrm{Im}(k_{Al})S}\times\left[1+\left|r_{\mathrm{vac.}\searrow\mathrm{Si}}\right|^2\exp\left(-2\mathrm{Im}(k_{Al})S\right)+\Psi(\varphi)\right]. \quad (4)$$

It is assumed that the lateral particle size does not vary along the direction vertical to the surface. With respect to Eq. (1) for thin films, the transmission factor $t_{\mathrm{Al}\nearrow\mathrm{vac.}}$ is equal to 1 since there is no sharp interface between the particle distribution and the vacuum and hence only the reflection on the bulk interface needs to be considered ($r_{\mathrm{Al}\nearrow\mathrm{vac.}}=0$). Further approximations to simplify Eq. (4), e.g., the non-consideration of the absorption effects inside the particles, can be found for small and large particle sizes S (on the nanometer-scale) in [104]. However, it turned out that even if the coverage is not continuous for some of the analyzed samples, the different Al patches are too close together to yield a typical island-like behavior in the angular intensity profile and Eq. (1) was sufficient to describe the experimental angular intensity profiles.

5. Results and discussion

The results extracted from the fits regarding the thickness, mass density, oxidation and the roughness of the layers are shown in Table 1.

Table 1
Numerical results with absolute uncertainties retrieved by means of the described fitting approach. T_{nom} is the nominal thickness, i.e., the thickness assuming a continuous layer of pure Al. T_{fit} stands for the fitted layer thickness, d_ρ for the relative decrement in density, $c_{Al_2O_3}$ for the relative oxide concentration, r_{Al} for the roughness. For some of the samples the K edge of the Al layer was also measured. The last sample corresponds to the Al_2O_3 sample prepared by the ESRF.

T_{nom} [nm]	T_{fit} [nm]	d_ρ	$c_{Al_2O_3}$	r_{Al} [nm]	K-edge [eV]
1	3.0/0.1	0.99/0.03	0.99/0.06	3.3/0.2	1565.8/0.8
5	6.0/0.2	0.98/0.01	0.46/0.02	3.2/0.2	1564.0/0.8
10	11.0/0.4	0.99/0.01	0.18/0.01	2.4/0.3	1562.6/0.8
20	17.8/0.5	0.98/0.01	0.06/0.01	1.2/0.6	1561.4/0.8
30	24.9/0.7	1.0/0.01	0.04/0.01	1.9/0.4	1561.1/0.8
50	43.7/2.0	1.0/0.01	0.06/0.01	3.2/0.6	1561.0/0.8
74	112.6/1.9	1.0/0.01	0.05/0.01	1.7/0.3	–
130	143.4/1.7	0.99/0.01	0.09/0.01	1.5/0.3	–
150	174.6/1.9	0.97/0.01	0.03/0.01	0.4/0.8	–
28	34.2/0.8	0.90/0.01	0.94/0.01	0/0	1564.4/0.8

The layer thickness deduced by the above described fitting approach can be directly compared to the nominal thickness which is the assumed thickness for a homogeneous, pure, nonoxidized and smooth layer with a continuous lateral distribution. The layer thicknesses deduced from the shape of the angular profiles are quite different from the assumed nominal thicknesses after the deposition process. However, in the latter only the mass of the deposit is surveyed and the layer thickness is derived by assuming a homogeneous deposition. But without the knowledge of the exact density of the layer, its surface roughness and taking possible oxidation effects

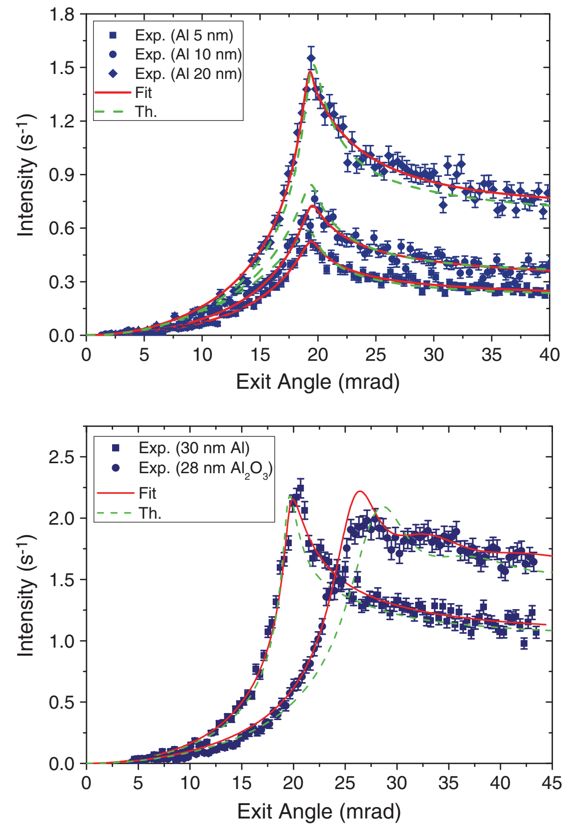

Fig. 8. Fitted experimental angular intensity curves for Al layers with 5, 10, and 20 nm nominal thickness (upper panel). In the lower panel the experimental results of an Al and an Al_2O_3 layer with nominal thicknesses of 30 nm and 28 nm, respectively, are also shown. It can be noted that, despite the Al and Al_2O_3 layers have comparable thicknesses, important differences in the features of the two angular profiles are observed. For comparison, the theoretical curves corresponding to pure and smooth layers having the same nominal thicknesses are also depicted.

http://doc.rero.ch

into account, the layer thickness cannot be properly derived from the deposited mass. Indeed, the physical surface morphology is different from the expectation of a homogeneous layer and may resemble more to an island-like distribution [17], especially for the thinnest layers. This can also be observed in Fig. 8 where the experimental curves significantly differ from the theoretical ones. The oxidation and the surface roughness have to be taken into account. Also the density does not necessarily correspond to the bulk value. The physical properties of a thin film can differ significantly from the bulk properties [105]. Thus, if only the deposited mass is known, the layer thickness can be underestimated. However, the layer density and the surface roughness can only be estimated by XRF-based methods if an angular intensity profile is acquired (XSW or GIXRF, GEXRF or also XRR). An accurate characterization of thin layers requires complementary measurements to the XRF spectrum at a single measurement position although high energy resolution spectroscopy allows to detect an energy shift due to chemical effects for transitions in which a valence shell is involved. From the thickness, density decrement and relative oxide concentration, the number of Al atoms per surface unit contained in the layers corresponding to the different samples can be recalculated. A good correlation with the nominally deposited number of atoms is found (Fig. 9).

Note that neither reference standard nor the knowledge of the instrumental response was needed to quantify the number of deposited Al atoms.

This quantification approach was cross-checked by means of a reference sample, a 15 keV Al-implanted Si wafer which was characterized in [48]. Usually, quantification measurements are realized by recording the XRF intensity at a single sample position and deducing the studied elemental quantity contained in the sample from the XRF intensity. These approaches are either based on a well characterized setup for reference-free quantification [106] or on a calibration of the setup by means of reference standards to determine the experimental response. For the present samples, the dose of the 15 keV Al-implanted sample, known from the reference-free quantification approach adopted by the Physikalisch Technische Bundesanstalt (PTB) [106], was used to determine the experimental response. The XRF intensities were then compared at a single exit angle which was identical for all samples. In grazing geometries, quantification measurements by recording the XRF intensity at a single grazing angle position can be either realized at the isokinetic angle ($\varphi_c/\sqrt{2}$) or at an angle far above the critical angle φ_c. If the XRF intensity is recorded at the isokinetic angle, the mass calibration curve may be subject to oscillations because of possible reflections at sharp sample interfaces [104]. Also absorption effects are more pronounced. Therefore, for the present samples, the XRF-based quantification was realized at the largest grazing emission angle, i.e., 40 mrad. Depending on the thickness of the deposited layer or its composition, X-ray absorption has also to be taken into account and calibration curves, i.e., the elemental mass versus the observed XRF intensity, are no more linear [104,107]. The limit, above which absorption effects can no more be safely neglected, is the critical thickness (Fig. 3). Above the critical thickness the fluorescence intensity deviates from the linear dependence on the number of emitting Al atoms and tends asymptotically to a maximal value with increasing layer thicknesses and eventual intensity contributions due to reflections at interfaces are considerably attenuated. For the implanted sample, the total implanted dose is within the critical thickness so that the influence of the bulk Si can be neglected while for the layered samples, the absorption of the emitted fluorescence signal can be readily corrected for by either assuming a pure Al layer on the top of the Si surface or by taking into account the matrix composition known from the GEXRF measurements. In Fig. 9 the results from the two quantification approaches, by means of fitting the shape of the angular intensity profile and by means of the XRF intensity once the instrumental response is known, are compared and a good overall agreement is observed. It appears also that the influence of the oxidation on the absorption correction is minor. This shows that the quantification of the deposited layers from the fits of the angular intensity curves, realized without calibration of the experimental response, is quite accurate. An advantage was certainly that all experimental parameters can be considered to be constant throughout an angular scan in GEXRF while with a grazing incidence technique the footprint of the beam and the rapidly changing solid angle have to be accounted for. The quantification by means of GEXRF presents therefore an interesting alternative to calibrate the experimental setup without using reference samples or vice-versa to characterize reference samples. Indeed, thin layers grown by a well-controlled method can be used as reference samples instead of the internal standard method or deposited droplets [108]. A characterization of these samples by means of GEXRF can be complementary to relative analytical methods.

In Fig. 10 the mass calibration for Al for the presented setup is shown which allows to quantify the number of atoms deposited on the bulk from the XRF intensity recorded at 40 mrad. At this angle

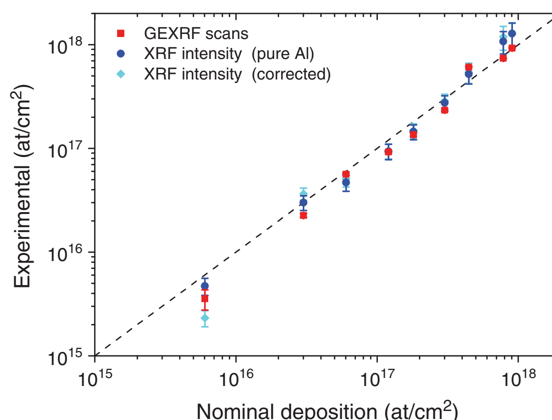

Fig. 9. Comparison of the GEXRF and XRF experimentally deduced number of Al atoms deposited per surface unit to the nominal value. A monolayer of Al atoms corresponds to $1.51*10^{15}$ at/cm^2. From the XRF intensity solely the amount of Al atoms in the layer can be estimated whereas the GEXRF measurements allow for a study of the surface distribution and quantification without setup calibration or reference samples.

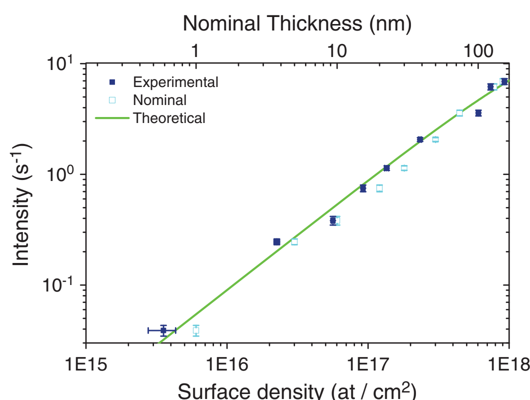

Fig. 10. Mass calibration curve of the experimental setup. The deposited mass per surface unit was deduced from the GEXRF curves without an instrumental calibration or a reference standard. The theoretical curve (solid line) fitted to the experimental values reproduces the variation of the scaling factor for the calculated grazing emission profiles for different thicknesses shown in the upper left panel of Fig. 5. The value extracted from this fit could also be used for the theoretical Al_2O_3 curve. The results for the nominally deposited mass, together with the nominal thickness (upper scale), are also shown.

http://doc.rero.ch

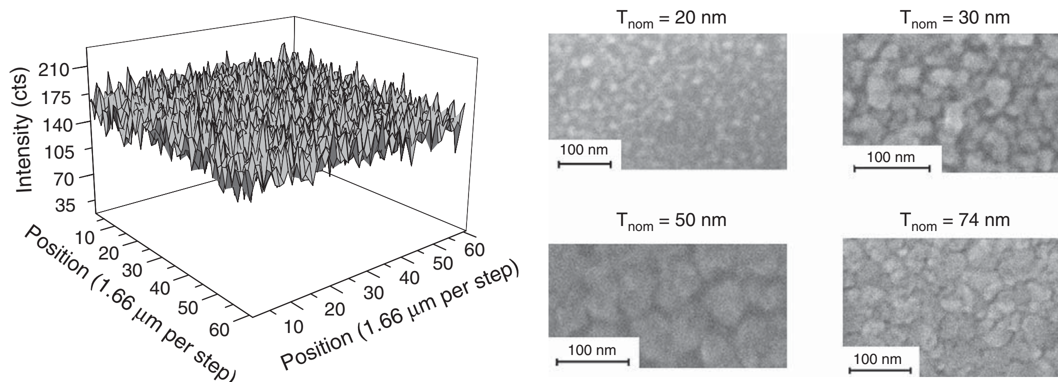

Fig. 11. Scan of the surface of the 30 nm thick Al-layered Si sample by means of μ-XRF (left side) and SEM pictures of the 20, 30, 50 and 74 nm thick Al-layered Si samples. The scale in the inset allows to estimate the size of the Al clusters which grow in size with the nominal thickness and start to interconnect.

the critical thickness for Al Kα is about 25 nm. The experimental response is implicitly accounted for by the scaling factor with respect to the theoretical curve and can be considered to be constant for all the angular scans. The nominal values correlate less well with the theoretical trend. For thicker layers, a deviation from linearity can be observed, as previously discussed. However, by quantifying the deposited mass solely with the XRF intensity recorded at a single position, the spatial distribution of the element of interest or the matrix in which it is embedded remains unknown without further measurements.

The Al layer roughness was for all analyzed samples except one found to be larger or equal to 1.5 nm, which indicates that the produced layers were quite rough. Indeed, the production of thin Al films with sub-nanometer roughness is still an active area of research [109,110] as the surface and interface roughnesses of metallic thin films have a direct impact on the performance, e.g., of the produced junction [111]. Regarding the correlation with the deposited Al amount, a trend of a decreasing roughness with increasing layer thickness can be observed. The large roughness for the thinnest samples indicates indirectly a non-continuous coverage of the Si surface by Al and an island-like surface morphology can be suspected. The surface roughness was qualitatively crosschecked with SEM for several samples (see Fig. 11). This surface-sensitive technique gives an image of the lateral surface structure without elemental or chemical discrimination but shows directly the surface roughness. However, a surface degradation caused probably by the heat load deposited by the electron beam was observed. For the thinner layer a cluster formation of

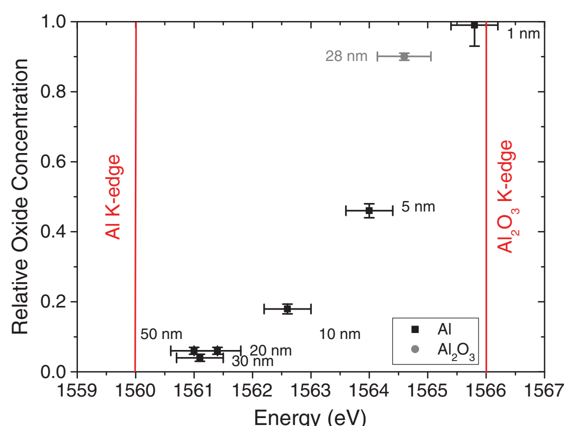

Fig. 12. Correlation plot between the relative oxide concentration retrieved by means of GEXRF and the Al K edge position measured by means of XANES for different Al layered Si samples, showing that GEXRF has also potential for chemical speciation.

Al can be observed, although the 1 and 5 nm Al-layered Si samples could not be analyzed by means of SEM due to lacking contrast in the recorded images. With increasing layer thickness, these clusters grow in size, covering altogether a larger surface and a coalescence of neighboring islands can be observed. For the 30 nm sample a percolation into an island network can be seen and it can be assumed that for even larger thicknesses a continuous film starts to grow. This behavior can be best explained by the Volmer–Weber model for thin film growth [105] in which, depending on the deposited mass, first grains of increasing size are observed before a laterally continuous film is grown. This behavior for Al deposited on Si was also observed in [17]. The samples with nominal thicknesses of 30 and 50 nm were also scanned by μ-XRF in the SXM chamber of the ID21 beamline (Fig. 11, 30 nm sample). A Ni mirror tilted at 7.5 mrad, the Si(111) double crystal monochromator with fixed exit angle and a Si mirror were used for these measurements performed at 7.5 keV. The focusing of the incident X-ray beam was realized with a zone plate and the beam size was 1.3×0.3 µm^2. The observed Al-Kα intensity is proportional to the deposited amount of Al and intensity variations can be correlated to the layer roughness if the layer density is assumed to be laterally constant. Taking into account the Poisson noise, the roughness was estimated to be 2.3 nm for the 30 nm sample and 3.4 nm for the 50 nm sample. These results are in agreement with the ones of the GEXRF measurements.

Moreover, the GEXRF angular profiles are sensitive to the presence of Al oxide. The aforementioned difference in the critical angles of pure Al and Al_2O_3 allows for an accurate estimation of the oxidation of the deposited Al layer. Indeed, the samples were not maintained in vacuum but exposed to ambient air in between the production and the analysis by GEXRF. It appears that the thinnest layer is fully oxidized and that with increasing layer thickness the concentration of Al_2O_3 with respect to Al decreases. These findings (Fig. 12 and Table 1) were confirmed for the Al-layered Si samples with thicknesses between 1 and 50 nm by XANES measurements performed at the ESRF ID21 beamline (the wiggler, the Si mirror tilted at 14 mrad, the NiB_4/C multilayer and a Si detector were used). This indicates that the oxidation process only affects the near-surface region of the deposited Al layers. Indeed, it is known that Al exposed to air at ambient temperatures oxidizes almost instantaneously at the surface; the oxide layer hinders, however, the diffusion of oxygen towards deeper lying Al atoms resulting in a lower oxidation rate of sub-surface regions [112]. In [113] it was pointed out that Al oxidation cannot only be found at the vacuum–Al layer interface on a range of 2 nm but also at the Al layer–Si bulk interface on a range of 1 nm due to the presence of a native Si oxide layer. These two considerations explain why the thinnest Al layer is almost fully oxidized and the decreasing ratio of Al_2O_3 to Al with increasing layer thickness to an asymptotic

http://doc.rero.ch

value. In the fitting approach described above a homogeneous mixture of Al and Al_2O_3 was assumed. Attempts to fit the experimental angular intensity profiles with a decreasing, depth-dependent (linear, logarithmic or exponential) mixing of Al_2O_3 and Al were not fruitful, the reason being probably the mentioned Al oxidation at the interface to the bulk Si. Allowing for different Al_2O_3 concentrations at the vacuum–Al layer interface and at the Al layer–Si bulk interface did not lead, for the thinner layers with a negligible self-absorption within the layer, to markedly different results in the ratio of Al_2O_3 to Al than the homogeneous mixture. Since the shape of the angular intensity curve is mainly influenced by the refraction processes at the sample interfaces, GEXRF is for thicker layers insensitive to the oxidation of Al in-between two interfaces as long as the complex refractive index does not diverge significantly from its value at the interface. Thus, the oxidation of the Al layers can only be ascertained by means of GEXRF in the vicinity of the interfaces of a layered system where the exact refractive index has to be taken into account in the fit. In contrast to GEXRF, XANES allows to study the entire volume of the thin Al layers at once. Al contaminations in the Si wafer can be neglected [43]. If, however, a depth-sensitive characterization of the chemical state is needed, the GEXRF technique can be combined with absorption techniques since the choice of the exit angle allows to select the depth-sensitivity of the setup (Fig. 3).

6. Conclusion and outlook

In summary, the mean layer composition in terms of thickness, density, oxidation and roughness of different Al films deposited on Si was reconstructed by means of the synchrotron radiation based high-energy-resolution GEXRF technique. The high brilliance and the energy-tunability of the synchrotron radiation source as well as the good background rejection capabilities and the high angular resolution of a wavelength-dispersive setup, namely the reflection-type curved crystal von Hamos spectrometer of the University of Fribourg, were of advantage for the experiment. The latter consisted in measuring the fluorescence intensity dependence of the Al Kα line on the grazing exit angle, defined relatively to the flat sample surface, in the range extending from 0 mrad to beyond the critical angle. As demonstrated, the angular intensity profiles allow for an accurate and reliable characterization, validated by complementary measurements, of surface layers of very small to intermediate layer thicknesses with a resolution on the sub-nanometer, respectively nanometer scale. A wide dynamic range for the number of atoms deposited on the Si surface can, thus, be covered. In addition, information on the surface distribution and oxidation can be extracted. It can thus be envisaged to monitor the dependence of these parameters on the production process parameters. Different thin film synthesis methods could also be compared. The presented setup has the potential for the analysis of a wide range of layered samples and to offer complementary information to other surface-sensitive methods for a full characterization of the surface layers or to serve simply as a cross-check tool. As an outlook the described synchrotron radiation based high-energy-resolution GEXRF technique could also be applied to multilayered samples or to study interdiffusion processes at the interfaces of a layered system. In the first case the necessary tools for data analysis can be retrieved in [101], in the latter case the sample has to be modeled with a stratified layer approach. A further extension to laterally inhomogeneous or well-structured samples, which cannot be accounted for by the presented theoretical model, can also be envisaged as with GIXRF [114]. Finally, because of the flexibility with respect to the elemental and chemical sample composition of XRF-based methods, the presented synchrotron radiation based high-energy-resolution GEXRF technique presents, in the case of single-layered samples where the refractive indexes of the different elements and compounds for the energy of interest are known and are sufficiently different from each other, the potential to contribute to the reliable investigation and characterization of technologically relevant samples, e.g., samples with high-k materials, or to contribute to the characterization of new reference materials.

http://doc.rero.ch

Acknowledgments

The financial support of the Swiss National Foundation is acknowledged. The authors would also like to thank the ESRF for supporting this experiment.

References

[1] M. Leskelä, M. Ritala, Atomic layer deposition (ALD): from precursors to thin film structures, Thin Solid Films 409 (1) (2002) 138–146, http://dx.doi.org/10.1016/S0040-6090(02)00117-7.

[2] J.E. Crowell, Chemical methods of thin film deposition: chemical vapor deposition, atomic layer deposition, and related technologies, J. Vac. Sci. Technol. A 21 (5) (2003) S88–S95, http://dx.doi.org/10.1116/1.1600451.

[3] J.R. Arthur, Molecular beam epitaxy, Surf. Sci. 500 (1–3) (2002) 189–217, http://dx.doi.org/10.1016/S0039-6028(01)01525-4.

[4] P. Kelly, R. Arnell, Magnetron sputtering: a review of recent developments and applications, Vacuum 56 (3) (2000) 159–172, http://dx.doi.org/10.1016/S0042-207X(99)00189-X.

[5] P.R. Willmott, J.R. Huber, Pulsed laser vaporization and deposition, Rev. Mod. Phys. 72 (2000) 315–328, http://dx.doi.org/10.1103/RevModPhys.72.315.

[6] P. Jiang, M.J. McFarland, Large-scale fabrication of wafer-size colloidal crystals, macroporous polymers and nanocomposites by spin-coating, J. Am. Chem. Soc. 126 (42) (2004) 13778–13786, http://dx.doi.org/10.1021/ja0470923.

[7] A. Jaworek, A. Sobczyk, Electrospraying route to nanotechnology: an overview, J. Electrost. 66 (3–4) (2008) 197–219, http://dx.doi.org/10.1016/j.elstat.2007.10.001.

[8] S.P. Murarka, Multilevel interconnections for ULSI and GSI era, Mater. Sci. Eng. 19 (3–4) (1997) 87–151, http://dx.doi.org/10.1016/S0927-796X(97)00002-8.

[9] J. Song, A.I. Inamdar, B. Jang, K. Jeon, Y. Kim, K. Jung, Y. Kim, H. Im, W. Jung, H. Kim, J.P. Hong, Effects of ultrathin Al layer insertion on resistive switching performance in an amorphous aluminum oxide resistive memory, Appl. Phys. Express 3 (9) (2010) 091101, http://dx.doi.org/10.1143/APEX.3.091101.

[10] K. Maekawa, K. Mori, N. Suzumura, K. Honda, Y. Hirose, K. Asai, A. Uedono, M. Kojima, Impact of Al in Cu alloy interconnects on electro and stress migration reliabilities, Microelectron. Eng. 85 (10) (2008) 2137–2141, http://dx.doi.org/10.1016/j.mee.2008.04.004.

[11] A. Debnath, N. Joshi, K. Muthe, J. Vyas, D. Aswal, S. Gupta, J. Yakhmi, Surface and electrical-transport studies of Ag/Al bilayer-structures grown by molecular beam epitaxy, Appl. Surf. Sci. 243 (1–4) (2005) 220–227, http://dx.doi.org/10.1016/j.apsusc.2004.09.066.

[12] D. Aswal, K. Muthe, N. Joshi, A. Debnath, S. Gupta, J. Yakhmi, In situ X-ray photoelectron spectroscopy of Ag/Al bilayers grown by molecular beam epitaxy, J. Cryst. Growth 256 (1–2) (2003) 201–205, http://dx.doi.org/10.1016/S0022-0248(03)01213-2.

[13] Y. Wang, T.L. Alford, Formation of aluminum oxynitride diffusion barriers for ag metallization, Appl. Phys. Lett. 74 (1) (1999) 52–54, http://dx.doi.org/10.1063/1.123130.

[14] F.-H. Lu, H.-D. Tsai, Y.-C. Chieh, Plasma oxidation of Al thin films on Si substrates, Thin Solid Films 516 (8) (2008) 1871–1876, http://dx.doi.org/10.1016/j.tsf.2007.09.049.

[15] A. Quade, H. Wulff, H. Steffen, T. Tun, R. Hippler, Investigation of the aluminium oxidation in an oxygen plasma excited by microwaves, Thin Solid Films 377–378 (2000) 626–630, http://dx.doi.org/10.1016/S0040-6090(00)01474-7.

[16] Z. Sun, C. Cao, L. Cao, P. Liang, X. Huang, X. Song, Surface morphology and optical properties of magnetron-sputtered ultrathin Al films, Vacuum 84 (6) (2010) 828–832, http://dx.doi.org/10.1016/j.vacuum.2009.11.002.

[17] N. Joshi, A. Debnath, D. Aswal, K. Muthe, M.S. Kumar, S. Gupta, J. Yakhmi, Morphology and resistivity of Al thin films grown on Si(111) by molecular beam epitaxy, Vacuum 79 (3–4) (2005) 178–185, http://dx.doi.org/10.1016/j.vacuum.2005.03.007.

[18] A. Zalar, J. Wang, Y. Zhao, E. Mittemeijer, P. Panjan, AES depth profiling of thermally treated Al/Si thin-film structures, Vacuum 71 (1–2) (2003) 11–17, http://dx.doi.org/10.1016/S0042-207X(02)00707-8.

[19] Y.J. Lee, S.-W. Kang, Study on the characteristics of aluminum thin films prepared by atomic layer deposition, J. Vac. Sci. Technol. A 20 (6) (2002) 1983–1988, http://dx.doi.org/10.1116/1.1513636.

[20] R.M. Gröger, M.R. Barczewski, Ultrathin Al layers on Si(111) and Si(100): structures and phase transitions, Surf. Interface Anal. 32 (1) (2001) 154–160, http://dx.doi.org/10.1002/sia.1027.

[21] A.E. Lita, J. John, E. Sanchez, Characterization of surface structure in sputtered Al films: correlation to microstructure evolution, J. Appl. Phys. 85 (2) (1999) 876–882, http://dx.doi.org/10.1063/1.369206.

[22] P. Williams, Secondary ion mass spectrometry, Annu. Rev. Mater. Sci. 15 (1) (1985) 517–548, http://dx.doi.org/10.1146/annurev.ms.15.080185.002505.

[23] R.N.S. Sodhi, Time-of-flight secondary ion mass spectrometry (TOF-SIMS): versatility in chemical and imaging surface analysis, Analyst 129 (2004) 483–487, http://dx.doi.org/10.1039/B402607C.

[24] M. Senoner, W.E.S. Unger, Sims imaging of the nanoworld: applications in science and technology, J. Anal. At. Spectrom. 27 (2012) 1050–1068, http://dx.doi.org/10.1039/C2JA30015J.

[25] W. Chu, J. Liu, Rutherford backscattering spectrometry: reminiscences and progresses, Mater. Chem. Phys. 46 (2–3) (1996) 183–188, http://dx.doi.org/10.1016/S0254-0584(97)80012-0.
[26] M. Copel, Medium-energy ion scattering for analysis of microelectronic materials, IBM J. Res. Dev. 44 (4) (2000) 571–582, http://dx.doi.org/10.1147/rd.444.0571.
[27] A.L. Tofterup, Theory of elastic and inelastic scattering of electrons emitted from solids: energy spectra and depth profiling in XPS/AES, Surf. Sci. 167 (1) (1986) 70–100, http://dx.doi.org/10.1016/0039-6028(86)90787-9.
[28] G.E. Jellison Jr., Generalized ellipsometry for materials characterization, Thin Solid Films 450 (1) (2004) 42–50, http://dx.doi.org/10.1016/j.tsf.2003.10.148.
[29] K. Vernon-Parry, Scanning electron microscopy: an introduction, III-Vs Rev. 13 (4) (2000) 40–44, http://dx.doi.org/10.1016/S0961-1290(00)80006-X.
[30] G. Binnig, H. Rohrer, C. Gerber, E. Weibel, Surface studies by scanning tunneling microscopy, Phys. Rev. Lett. 49 (1982) 57–61, http://dx.doi.org/10.1103/PhysRevLett.49.57.
[31] J. Miranda, J. Rickards, R. Trejo-Luna, Pixe depth profiling using variation of detection angle, Nucl. Instr. Meth. B 249 (1–2) (2006) 394–396, http://dx.doi.org/10.1016/j.nimb.2006.04.062.
[32] D. Abou-Ras, R. Caballero, C.-H. Fischer, C. Kaufmann, I. Lauermann, R. Mainz, H. Mönig, A. Schöpke, C. Stephan, C. Streeck, S. Schorr, A. Eicke, M. Döbeli, B. Gade, J. Hinrichs, T. Nunney, H. Dijkstra, V. Hoffmann, D. Klemm, V. Efimova, A. Bergmaier, G. Dollinger, T. Wirth, W. Unger, A. Rockett, A. Perez-Rodriguez, J. Alvarez-Garcia, V. Izquierdo-Roca, T. Schmid, P.-P. Choi, M. Müller, F. Bertram, J. Christen, H. Khatri, R. Collins, S. Marsillac, I. Kötschau, Comprehensive comparison of various techniques for the analysis of elemental distributions in thin films, Microsc. Microanal. 17 (2011) 728–751.
[33] C. Adelmann, T. Conard, A. Franquet, B. Brijs, F. Munnik, S. Burgess, T. Witters, J. Meersschaut, J.A. Kittl, W. Vandervorst, S.V. Elshocht, Compositional depth profiling of TaCN thin films, J. Vac. Sci. Technol. A 30 (4) (2012) 041510, http://dx.doi.org/10.1116/1.4726261.
[34] S. Hofmann, Ultimate depth resolution and profile reconstruction in sputter profiling with AES and SIMS, Surf. Interface Anal. 30 (1) (2000) 228–236, http://dx.doi.org/10.1002/1096-9918(200008)30:1<228::AID-SIA821>3.0.CO;2-E.
[35] R. Escobar Galindo, R. Gago, D. Duday, C. Palacio, Towards nanometric resolution in multilayer depth profiling: a comparative study of RBS, SIMS, XPS and GDOES, Anal. Bioanal. Chem. 396 (2010) 2725–2740, http://dx.doi.org/10.1007/s00216-009-3339-y.
[36] S. Oswald, S. Baunack, Comparison of depth profiling techniques using ion sputtering from the practical point of view, Thin Solid Films 425 (2003) 9–19.
[37] O. Baake, P. Hoffmann, S. Flege, H. Ortner, S. Gottschalk, W. Berky, A. Balogh, W. Ensinger, B. Beckhoff, M. Kolbe, M. Gerlach, B. Pollakowski, J. Weser, G. Ulm, M. Haschke, E. Blokhina, M. Peter, D. Porta, M. Heck, Nondestructive characterization of nanoscale layered samples, Anal. Bioanal. Chem. 393 (2009) 623–634, http://dx.doi.org/10.1007/s00216-008-2465-2.
[38] C. Streli, G. Pepponi, P. Wobrauschek, N. Zöger, P. Pianetta, K. Baur, S. Pahlke, L. Fabry, C. Mantler, B. Kanngießer, W. Malzer, Analysis of low Z elements on Si wafer surfaces with synchrotron radiation induced total reflection X-ray fluorescence at SSRL, Beamline 3-3: comparison of droplets with spin coated wafers, Spectrochim. Acta B 58 (12) (2003) 2105–2112, http://dx.doi.org/10.1016/S0584-8547(03)00218-0.
[39] S. Pahlke, Quo vadis total reflection X-ray fluorescence? Spectrochim. Acta B 58 (12) (2003) 2025–2038, http://dx.doi.org/10.1016/S0584-8547(03)00193-9.
[40] K. Baur, S. Brennan, P. Pianetta, R. Opila, Looking at trace impurities on silicon wafers with synchrotron radiation, Anal. Chem. 74 (23) (2002) 608 A–616 A, http://dx.doi.org/10.1021/ac022159v.
[41] S. Pahlke, L. Fabry, L. Kotz, C. Mantler, T. Ehmann, Determination of ultra trace contaminants on silicon wafer surfaces using total-reflection X-ray fluorescence TXRF 'state-of-the-art', Spectrochim. Acta B 56 (11) (2001) 2261–2274, http://dx.doi.org/10.1016/S0584-8547(01)00312-3.
[42] J. Szlachetko, D. Banaś, A. Kubala-Kukuś, M. Pajek, W. Cao, J.-Cl. Dousse, J. Hoszowska, Y. Kayser, M. Szlachetko, M. Kavčič, M. Salome, J. Susini, Application of the high-resolution grazing-emission X-ray fluorescence method for impurities control in semiconductor nanotechnology, J. Appl. Phys. 105 (8) (2009) 086101, http://dx.doi.org/10.1063/1.3086658.
[43] A. Kubala-Kukuś, D. Banaś, W. Cao, J.-Cl. Dousse, J. Hoszowska, Y. Kayser, M. Pajek, M. Salomé, J. Susini, J. Szlachetko, M. Szlachetko, Observation of ultralow-level Al impurities on a silicon surface by high-resolution grazing emission X-ray fluorescence excited by synchrotron radiation, Phys. Rev. B 80 (11) (2009) 113305, http://dx.doi.org/10.1103/PhysRevB.80.113305.
[44] S. de Gendt, K. Kenis, M. Baeyens, P. Mertens, M. Heyns, G. Wiener, S. Kidd, D. Knotter, P. de Bokx, Silicon surface metal contamination measurements using grazing-emission XRF spectrometry, Mater. Res. Soc. Symp. Proc. 477 (1997) 397–402.
[45] G. Pepponi, D. Giubertoni, M. Bersani, F. Meirer, D. Ingerle, G. Steinhauser, C. Streli, P. Hoenicke, B. Beckhoff, Grazing incidence X-ray fluorescence and secondary ion mass spectrometry combined approach for the characterization of ultrashallow arsenic distribution in silicon, J. Vac. Sci. Technol. B 28 (1) (2010), http://dx.doi.org/10.1116/1.3292647, C1C59-C1C64.
[46] P. Hönicke, B. Beckhoff, M. Kolbe, D. Giubertoni, J. van den Berg, G. Pepponi, Depth profile characterization of ultra shallow junction implants, Anal. Bioanal. Chem. 396 (2010) 2825–2832, http://dx.doi.org/10.1007/s00216-009-3266-y.
[47] Y. Kayser, D. Banaś, W. Cao, J.-Cl. Dousse, J. Hoszowska, P. Jagodziński, M. Kavčič, A. Kubala-Kukuś, S. Nowak, M. Pajek, J. Szlachetko, Depth profiling of dopants implanted in Si using the synchrotron radiation based high-resolution grazing emission technique, X-Ray Spectrom. 41 (2) (2012) 98–104, http://dx.doi.org/10.1002/xrs.2372.
[48] P. Hönicke, Y. Kayser, B. Beckhoff, M. Muller, J.-Cl. Dousse, J. Hoszowska, S.H. Nowak, Characterization of ultra-shallow aluminum implants in silicon by grazing incidence and grazing emission X-ray fluorescence spectroscopy, J. Anal. At. Spectrom. 27 (2012) 1432–1438, http://dx.doi.org/10.1039/C2JA10385K.
[49] F. Meirer, A. Singh, P. Pianetta, G. Pepponi, F. Meirer, C. Streli, T. Homma, Synchrotron radiation-induced total reflection X-ray fluorescence analysis, TrAC-Trend Anal. Chem. 29 (6) (2010) 479–496, http://dx.doi.org/10.1016/j.trac.2010.04.001.
[50] A. von Bohlen, Total reflection X-ray fluorescence and grazing incidence X-ray spectrometry — tools for micro- and surface analysis. A review, Spectrochim. Acta B 64 (9) (2009) 821–832, http://dx.doi.org/10.1016/j.sab.2009.06.012.
[51] P. Wobrauschek, Total reflection X-ray fluorescence analysis: a review, X-Ray Spectrom. 36 (5) (2007) 289–300, http://dx.doi.org/10.1002/xrs.985.
[52] R. Klockenkämper, M. Becker, A. von Bohlen, H.W. Becker, H. Krzyzanowska, L. Palmetshofer, Near-surface density of ion-implanted Si studied by Rutherford backscattering and total-reflection X-ray fluorescence, J. Appl. Phys. 98 (3) (2005) 033517, http://dx.doi.org/10.1063/1.1997289.
[53] M. Claes, P. de Bokx, N. Willard, P. Veny, R. Van Grieken, Optimization of sample preparation for grazing emission X-ray fluorescence in micro- and trace analysis applications, Spectrochim. Acta B 52 (7) (1997) 1063–1070, http://dx.doi.org/10.1016/S0584-8547(96)01654-0.
[54] R.S. Becker, J.A. Golovchenko, J.R. Patel, X-ray evanescent-wave absorption and emission, Phys. Rev. Lett. 50 (3) (1983) 153–156, http://dx.doi.org/10.1103/PhysRevLett.50.153.
[55] M. Krämer, A. von Bohlen, C. Sternemann, M. Paulus, R. Hergenröder, Synchrotron radiation induced X-ray standing waves analysis of layered structures, Appl. Surf. Sci. 253 (7) (2007) 3533–3542, http://dx.doi.org/10.1016/j.apsusc.2006.07.076.
[56] R. Unterumsberger, B. Pollakowski, M. Müller, B. Beckhoff, Complementary characterization of buried nanolayers by quantitative X-ray fluorescence spectrometry under conventional and grazing incidence conditions, Anal. Chem. 83 (22) (2011) 8623–8628, http://dx.doi.org/10.1021/ac202074s.
[57] H.J. Sánchez, C.A. Pérez, Study of copper surface oxidation by grazing angle X-ray excitation, Spectrochim. Acta B 65 (6) (2010) 466–470, http://dx.doi.org/10.1016/j.sab.2010.02.018.
[58] H.J. Sanchez, C.A. Perez, R.D. Perez, M. Rubio, Surface analysis by total-reflection X-ray fluorescence, Radiat. Phys. Chem. 48 (3) (1996) 325–331, http://dx.doi.org/10.1016/0969-806X(95)00454-6.
[59] U. Weisbrod, R. Gutschke, J. Knoth, H. Schwenke, Total reflection X-ray fluorescence spectrometry for quantitative surface and layer analysis, Appl. Phys. A: Mater. 53 (1991) 449–456.
[60] D.K.G. de Boer, Glancing-incidence X-ray fluorescence of layered materials, Phys. Rev. B 44 (2) (1991) 498–511, http://dx.doi.org/10.1103/PhysRevB.44.498.
[61] M. Krämer, A. von Bohlen, C. Sternemann, M. Paulus, R. Hergenroder, X-ray standing waves: a method for thin layered systems, J. Anal. At. Spectrom. 21 (2006) 1136–1142, http://dx.doi.org/10.1039/B607252F.
[62] K. Tsuji, T. Yamada, T. Utaka, K. Hirokawa, The effects of surface roughness on the angle-dependent total-reflection X-ray fluorescence of ultrathin films, J. Appl. Phys. 78 (2) (1995) 969–973, http://dx.doi.org/10.1063/1.360291.
[63] H. Schwenke, R. Gutschke, J. Knoth, M. Kock, Treatment of roughness and concentration gradients in total reflection X-ray fluorescence analysis of surfaces, Appl. Phys. A: Mater. 54 (1992) 460–465.
[64] L.G. Parratt, Surface studies of solids by total reflection of X-rays, Phys. Rev. 95 (2) (1954) 359–369, http://dx.doi.org/10.1103/PhysRev.95.359.
[65] H. Jiang, J. Zhu, J. Xu, X. Wang, Z. Wang, M. Watanabe, Determination of layer-thickness variation in periodic multilayer by X-ray reflectivity, J. Appl. Phys. 107 (10) (2010) 103523, http://dx.doi.org/10.1063/1.3383037.
[66] M. Kolbe, B. Beckhoff, M. Krumrey, G. Ulm, Comparison of reference-free X-ray fluorescence analysis and X-ray reflectometry for thickness determination in the nanometer range, Appl. Surf. Sci. 252 (1) (2005) 49–52, http://dx.doi.org/10.1016/j.apsusc.2005.01.11, (13th Applied Surface Analysis Workshop. AOFA 13).
[67] M. Krumrey, M. Hoffmann, G. Ulm, K. Hasche, P. Thomsen-Schmidt, Thickness determination for SiO_2 films on Si by X-ray reflectometry at the Si K edge, Thin Solid Films 459 (1–2) (2004) 241–244, http://dx.doi.org/10.1016/j.tsf.2003.12.100.
[68] S.K. Ghose, B.N. Dev, X-ray standing wave and reflectometric characterization of multilayer structures, Phys. Rev. B 63 (24) (2001) 245409, http://dx.doi.org/10.1103/PhysRevB.63.245409.
[69] H.P. Urbach, P.K. de Bokx, Calculation of intensities in grazing-emission X-ray fluorescence, Phys. Rev. B 53 (7) (1996) 3752–3763, http://dx.doi.org/10.1103/PhysRevB.53.3752.
[70] I. Koshelev, A. Paulikas, M. Beno, G. Jennings, J. Linton, M. Grimsditch, S. Uran, B. Veal, Chromium-oxide growth on Fe–Ni–Cr alloy studied with grazing-emission X-ray fluorescence, Oxid. Met. 68 (15) (2007) 37–51, http://dx.doi.org/10.1007/s11085-007-9053-2.
[71] M.L. Monaghan, T. Nigam, M. Houssa, S.D. Gendt, H.P. Urbach, P.K. de Bokx, Characterization of silicon oxynitride films by grazing-emission X-ray fluorescence spectrometry, Thin Solid Films 359 (2) (2000) 197–202, http://dx.doi.org/10.1016/S0040-6090(99)00739-7.
[72] K. Tsuji, H. Takenaka, K. Wagatsuma, P.K. de Bokx, R. Van Grieken, Enhancement of X-ray fluorescence intensity from an ultra-thin sandwiched layer at grazing-emission angles, Spectrochim. Acta B 54 (13) (1999) 1881–1888, http://dx.doi.org/10.1016/S0584-8547(99)00143-3.
[73] G. Wiener, S.J. Kidd, C.A.H. Mutsaers, R.A.M. Wolters, P.K. de Bokx, Characterization of titanium nitride layers by grazing-emission X-ray fluorescence spectrometry, Appl. Surf. Sci. 125 (2) (1998) 129–136, http://dx.doi.org/10.1016/S0169-4332(97)00412-1.
[74] P. de Bokx, C. Kok, A. Bailleul, G. Wiener, H. Urbach, Grazing-emission X-ray fluorescence spectrometry; principles and applications, Spectrochim. Acta B 52 (7) (1997) 829–840, http://dx.doi.org/10.1016/S0584-8547(96)01644-8.

http://doc.rero.ch

[75] T. Noma, A. Iida, K. Sakurai, Fluorescent-X-ray-interference effect in layered materials, Phys. Rev. B 48 (23) (1993) 17524–17526, http://dx.doi.org/10.1103/PhysRevB.48.17524.

[76] F. Meirer, G. Pepponi, C. Streli, P. Wobrauschek, N. Zoeger, Grazing exit versus grazing incidence geometry for X-ray absorption near edge structure analysis of arsenic traces, J. Appl. Phys. 105 (7) (2009) 074906, http://dx.doi.org/10.1063/1.3106086.

[77] J. Yang, K. Tsuji, X. Lin, D. Han, X. Ding, A micro X-ray fluorescence analysis method using polycapillary X-ray optics and grazing exit geometry, Thin Solid Films 517 (11) (2009) 3357–3361, http://dx.doi.org/10.1016/j.tsf.2008.12.004.

[78] T. Emoto, Y. Sato, Y. Konishi, X. Ding, K. Tsuji, Development and applications of grazing exit micro X-ray fluorescence instrument using a polycapillary X-ray lens, Spectrochim. Acta B 59 (8) (2004) 1291–1294, http://dx.doi.org/10.1016/j.sab.2004.05.016.

[79] K. Tsuji, M. Huisman, Z. Spolnik, K. Wagatsuma, Y. Mori, R. Van Grieken, R.D. Vis, Comparison of grazing-exit particle-induced X-ray emission with other related methods, Spectrochim. Acta B 55 (7) (2000) 1009–1016, http://dx.doi.org/10.1016/S0584-8547(00)00148-8.

[80] K. Tsuji, Grazing-exit electron probe X-ray microanalysis (GE-EPMA): fundamental and applications, Spectrochim. Acta B 60 (11) (2005) 1381–1391, http://dx.doi.org/10.1016/j.sab.2005.08.013.

[81] Z.M. Spolnik, M. Claes, R. Van Grieken, Determination of trace elements in organic matrices by grazing-emission X-ray fluorescence spectrometry, Anal. Chim. Acta 401 (1–2) (1999) 293–298, http://dx.doi.org/10.1016/S0003-2670(99)00471-7.

[82] R. Klockenkämper, A. von Bohlen, Determination of the critical thickness and the sensitivity for thin-film analysis by total reflection X-ray fluorescence spectrometry, Spectrochim. Acta B 44 (5) (1989) 461–469, http://dx.doi.org/10.1016/0584-8547(89)80051-5.

[83] K. Tsuji, S. Sato, K. Hirokawa, Glancing-incidence and glancing-takeoff X-ray fluorescence analysis of a Mn ultrathin film on an Au layer, Thin Solid Films 274 (1–2) (1996) 18–22, http://dx.doi.org/10.1016/0040-6090(95)07082-6.

[84] Y.C. Sasaki, Y. Suzuki, Y. Tomioka, A. Fukuhara, Observation of an interference effect for fluorescent X rays, Phys. Rev. B 48 (10) (1993) 7724–7726, http://dx.doi.org/10.1103/PhysRevB.48.7724.

[85] C. Maurizio, M. Rovezzi, F. Bardelli, H.G. Pais, F. D'Acapito, Setup for optimized grazing incidence X-ray absorption experiments on thin films on substrates, Rev. Sci. Instrum. 80 (6) (2009) 063904, http://dx.doi.org/10.1063/1.3155791.

[86] B. Pollakowski, B. Beckhoff, F. Reinhardt, S. Braun, P. Gawlitza, Speciation of deeply buried TiOx nanolayers with grazing-incidence X-ray fluorescence combined with a near-edge X-ray absorption fine-structure investigation, Phys. Rev. B 77 (23) (2008) 235408, http://dx.doi.org/10.1103/PhysRevB.77.235408.

[87] G.A. Waychunas, Grazing-incidence X-ray absorption and emission spectroscopy, Rev. Mineral. Geochem. 49 (1) (2002) 267–315, http://dx.doi.org/10.2138/gsrmg.49.1.267.

[88] K. Shinoda, S. Sato, S. Suzuki, T. Uruga, H. Tanida, H. Toyokawa, Y. Terada, Y. Takagaki, Nondestructive depth resolved analysis by using grazing exit fluorescence-yield X-ray absorption spectroscopy, J. Surf. Anal. 15 (3) (2009) 295–298.

[89] Y. Suzuki, Surface extended X-ray-absorption fine-structure spectroscopy measurement using the evanescent-wave effect of fluorescent X-ray, Phys. Rev. B 39 (5) (1989) 3393–3395, http://dx.doi.org/10.1103/PhysRevB.39.3393.

[90] Y. Fujii, E. Yanase, K. Nishio, A proposal of depth profile analysis method of strain distribution in surface layer using X-ray diffraction at small glancing angles of incidence, J. Phys. Conf. Ser. 83 (2007) 012008, http://dx.doi.org/10.1088/1742-6596/83/1/012008.

[91] G.H. Vineyard, Grazing-incidence diffraction and the distorted-wave approximation for the study of surfaces, Phys. Rev. B 26 (8) (1982) 4146–4159, http://dx.doi.org/10.1103/PhysRevB.26.4146.

[92] T. Noma, K. Takada, A. Iida, Surface-sensitive X-ray fluorescence and diffraction analysis with grazing-exit geometry, X-Ray Spectrom. 28 (6) (1999) 433–439, http://dx.doi.org/10.1002/(SICI)1097-4539(199911/12)28:6<433::AID-XRS386>3.0.CO;2-C.

[93] J. Hoszowska, J.-Cl. Dousse, J. Kern, C. Rhême, High-resolution von Hamos crystal X-ray spectrometer, Nucl. Instrum. Meth. A 376 (1) (1996) 129–138, http://dx.doi.org/10.1016/0168-9002(96)00262-8.

[94] J. Szlachetko, J.-Cl. Dousse, J. Hoszowska, M. Berset, W. Cao, M. Szlachetko, M. Kavčič, Relative detection efficiency of back- and front-illuminated charge-coupled device cameras for X-rays between 1 kev and 18 kev, Rev. Sci. Instrum. 78 (9) (2007) 093102, http://dx.doi.org/10.1063/1.2779214.

[95] J. Szlachetko, J.-Cl. Dousse, J. Hoszowska, M. Pajek, R. Barrett, M. Berset, K. Fennane, A. Kubala-Kukuś, M. Szlachetko, High-resolution study of X-ray resonant Raman scattering at the K edge of silicon, Phys. Rev. Lett. 97 (7) (2006) 073001, http://dx.doi.org/10.1103/PhysRevLett.97.073001.

[96] M. Kavčič, M. Zitňik, K. Bucar, J. Szlachetko, Application of wavelength dispersive X-ray spectroscopy to improve detection limits in X-ray analysis, X-Ray Spectrom. 40 (1) (2011) 2–6, http://dx.doi.org/10.1002/xrs.1291.

[97] M.K. Tiwari, G.S. Lodha, K.J.S. Sawhney, Applications of the 'CATGIXRF' computer program to the grazing incidence X-ray fluorescence and X-ray reflectivity characterization of thin films and surfaces, X-Ray Spectrom. 39 (2) (2010) 127–134, http://dx.doi.org/10.1002/xrs.1215.

[98] R.D. Pérez, H. Sánchez, M. Rubio, Efficient calculation method for glancing angle X-ray techniques, X-Ray Spectrom. 31 (4) (2002) 296–299, http://dx.doi.org/10.1002/xrs.557.

[99] R.D. Pérez, H.J. Sánchez, M. Rubio, Theoretical model for the calculation of interference effects in TXRF and GEXRF, X-Ray Spectrom. 30 (5) (2001) 292–295, http://dx.doi.org/10.1002/xrs.500.

[100] D.L. Windt, IMD-software for modeling the optical properties of multilayer films, Comput. Phys. 12 (1998) 360–370, http://dx.doi.org/10.1063/1.168689.

[101] H.P. Urbach, P.K. de Bokx, Grazing emission X-ray fluorescence from multilayers, Phys. Rev. B 63 (8) (2001) 085408, http://dx.doi.org/10.1103/PhysRevB.63.085408.

[102] D.K.G. Boer, A.J.G. Leenaers, W.W. Hoogenhof, The profile of layered materials reflected by glancing-incidence X-ray analysis, Appl. Phys. A: Mater. 58 (1994) 169–172.

[103] D.K.G. de Boer, X-ray scattering and X-ray fluorescence from materials with rough interfaces, Phys. Rev. B 53 (10) (1996) 6048–6064, http://dx.doi.org/10.1103/PhysRevB.53.6048.

[104] Z.M. Spolnik, M. Claes, R.E. Van Grieken, P.K. de Bokx, H.P. Urbach, Quantification in grazing-emission X-ray fluorescence spectrometry, Spectrochim. Acta B 54 (10) (1999) 1525–1537, http://dx.doi.org/10.1016/S0584-8547(99)00051-8.

[105] N. Kaiser, Review of the fundamentals of thin-film growth, Appl. Opt. 41 (16) (2002) 3053–3060, http://dx.doi.org/10.1364/AO.41.003053.

[106] B. Beckhoff, R. Fliegauf, M. Kolbe, M. Müller, J. Weser, G. Ulm, Reference-free total reflection X-ray fluorescence analysis of semiconductor surfaces with synchrotron radiation, Anal. Chem. 79 (20) (2007) 7873–7882, http://dx.doi.org/10.1021/ac071236p.

[107] A. Kuczumow, M. Schmeling, R. Van Grieken, Critical assessment and proposal for reconstruction of a grazing emission X-ray fluorescence instrument, J. Anal. At. Spectrom. 15 (2000) 535–542, http://dx.doi.org/10.1039/A908661G.

[108] S.W. Gaarenstroom, Growth and characterization of aluminum oxide thin films for evaluation as reference materials, J. Vac. Sci. Technol. A 15 (3) (1997) 470–477, http://dx.doi.org/10.1116/1.580876.

[109] D.L. Rode, V.R. Gaddam, J.H. Yi, Subnanometer surface roughness of dc magnetron sputtered Al films, J. Appl. Phys. 102 (2) (2007) 024303, http://dx.doi.org/10.1063/1.2756039.

[110] I. Levine, A. Yoffe, A. Salomon, W. Li, Y. Feldman, A. Vilan, Epitaxial two dimensional aluminum films on silicon (111) by ultra-fast thermal deposition, J. Appl. Phys. 111 (12) (2012) 124320, http://dx.doi.org/10.1063/1.4730411.

[111] C.W. Miller, Z.-P. Li, J. Akerman, I.K. Schuller, Impact of interfacial roughness on tunneling conductance and extracted barrier parameters, Appl. Phys. Lett. 90 (4) (2007) 043513, http://dx.doi.org/10.1063/1.2431443.

[112] N. Cabrera, N.F. Mott, Theory of the oxidation of metals, Rep. Prog. Phys. 12 (1) (1949) 163.

[113] A. Quade, H. Wulff, Investigation of oxidation process on plasma treated thin Al-films by GIXR and GIXRD, Thin Solid Films 355–356 (1999) 494–499, http://dx.doi.org/10.1016/S0040-6090(99)00553-2.

[114] P. Hönicke, B. Beckhoff, M. Kolbe, S. List, T. Conard, H. Struyff, Depth-profiling of vertical sidewall nanolayers on structured wafers by grazing incidence X-ray fluorescence, Spectrochim. Acta B 63 (12) (2008) 1359–1364, http://dx.doi.org/10.1016/j.sab.2008.10.005.

http://doc.rero.ch